DOE/AL/38027--T4

The Pennsylvania State University

The Graduate School

DOE/AL/38027--T4

DE92 006766

IGNITION FLAME KERNEL GROWTH UNDER SIMULATED IDLE CONDITIONS

A Thesis in

Mechanical Engineering

by

Thomas J. Legutko

Submitted in Partial Fulfillment
of the Requirements
for the Degree of

Master of Science

May 1990

I grant The Pennsylvania State University the nonexclusive right to use this work for the University's own purposes and to make single copies of the work available to the public on a not-for-profit basis if copies are not otherwise available.

Thomas J. Legutko

Thomas J. Legutko

DISCLAIMER

We approve the thesis of Thomas J. Legutko.

Date of Signature

Domenic A. Santavicca — 2/6/90
Domenic A. Santavicca
Associate Professor of
Mechanical Engineering
Thesis Advisor

Thomas A. Litzinger — 2/5/90
Thomas A. Litzinger
Assistant Professor of
Mechanical Engineering

Harold R. Jacobs — 2/5/90
Harold R. Jacobs
Professor of Mechanical
Engineering
Head of the Department
of Mechanical Engineering

ABSTRACT

The intent of this thesis was to characterize the effects of dilution, turbulence, and ignition system power on early flame kernel growth, and its cycle-to-cycle variations. The experiments were conducted in a turbulent flow reactor capable of supplying a propane-air mixture with an equivalence ratio of 1.0, and nitrogen dilutions of 0% and 15% by volume. The effects of turbulence were characterized using a constant mean flow of 1.25 m/s with two turbulence intensities, 24% and 77% of the mean flow. The total ignition energy of the experiment was held at approximately 60 mJ. However, the power level and consequently the duration of the spark was varied.

The results showed that the cycle-to-cycle variations experienced by the flame kernel can be reduced by choosing an appropriate ignition system. For mixtures with high turbulence levels, faster and more repeatable growth rates were observed with an enhanced breakdown ignition system. However, for low turbulence mixtures, an inductive ignition system, even though possessing a slower growth rate than the enhanced breakdown system, showed fewer cycle-to-cycle variations.

TABLE OF CONTENTS

LIST OF FIGURES

FIGURE

FIGURE

FIGURE

FIGURE

LIST OF TABLES

ACKNOWLEDGMENTS

The author thanks Professor Domenic A. Santavicca, his thesis advisor, for the opportunity to conduct this research. He also thanks Dr. Richard W. Anderson, of Ford Motor Company, for his patience and invaluable assistance in helping the author design the ignition systems used in the experiment. Special gratitude goes to future Dr. Chi M. Ho, whose suggestions and assistance made this thesis possible.

Render, therefore, to Caesar the things that are Caesar's; and to God, the things that are God's.

- Mark 12:17

Chapter 1

INTRODUCTION

1.1 Motivation: Dilute Charge Ignition

Ongoing research in the automotive industry has been concerned with improving fuel economy under the constraints of strict emission standards. One method of attacking this problem is the use of charge dilution. Charge dilution offers the potential for improved engine efficiency, and can lead to reductions of nitric oxide emissions due to lower combustion temperatures.

There are three ways to achieve charge dilution on automotive engines: exhaust gas recirculation (EGR), lean operation, and incomplete exhaust gas scavenging. Current automobile manufacturers all use the concept of charge dilution to reduce nitric oxide emissions. All engine manufacturers, except Volkswagen, accomplish this by operating their engines at an equivalence ratio of 1.0, and using EGR dilution. Volkswagen uses the lean operation concept to reduce nitric oxide emissions.

Even though charge dilution does reduce NO_x emissions, it does have disadvantages. First, lower combustion temperatures result in lower flame speeds, and in turn lower burn rates. This leads to incomplete combustion of the charge and increased hydrocarbon

emissions. Second, dilute charges are very susceptible to misfires and cycle-to-cycle variations in the combustion process, which lowers the efficiency and again increases hydrocarbon emissions. These variations are especially prominent at idle operation, where charge dilution is due to incomplete cylinder scavenging, and results in what is usually referred to as engine roughness.

At idle operation, spark timing for current automotive engines is advanced up to 30 degrees BTDC, to compensate for the effects of dilution, which can be as high as 30% by volume. This spark advance results in relatively low temperatures and low pressures at the time of ignition, which makes the ignition process more difficult. Under these conditions engine roughness results from the slow and non-repeatable growth of the ignition kernel.

1.2 Approach

The focus of this study was to investigate early flame kernel growth under simulated idle conditions where cycle-to-cycle variations are most prominent. The experiments were conducted in a turbulent flow reactor under conditions which simulate the turbulent flow field in an engine at idle operation. A propane-air mixture of equivalence ratio 1.0 was used at a pressure of 1

atmosphere, and temperature of 300 K. These conditions approximate the conditions found in a spark engine at idle, where the equivalence ratio is 1.0, the pressure is near 2 atmospheres, and the temperature is approximately 500 K.

Of particular interest were the effects of charge dilution, turbulence, and ignition power on ignition flame kernel growth and its variation. Both 0% and 15% dilution conditions (with nitrogen) were studied, in comparison to actual engines where dilution ranges from 0% to 30% at idle. The effects of turbulence were also studied using two different flow conditions. The first case consisted of a mean velocity of 1.25 m/sec and a turbulence intensity of .3 m/sec. For the second case the same mean velocity was used but the turbulence intensity was increased to .96 m/sec. For both cases the turbulence integral length scale was approximately 3 mm. These turbulence conditions are representative of those in an actual engine at idle. Ignition was achieved with a standard automotive system modified to provide sparks of fixed total energy but with variable power levels and durations. Measurements of flame kernel growth were made using high speed laser shadowgraphy. The images from the shadowgraphy were analyzed to obtain the equivalent flame kernel radius versus time.

1.3 Goals of This Research

The goal of this project was to characterize the effects of dilution, turbulence, and ignition system power on early flame kernel growth, and the cycle-to-cycle variations of the flame kernel growth rate. The basic approach was to determine the operating conditions with and without dilution which will yield the fastest and most repeatable kernel growth rates resulting in lower cycle-to-cycle variations.

Chapter 2

BACKGROUND

2.1 Characteristics of Ignition Sparks

To understand the nature of spark ignition, the physical properties of the spark itself [1, 2, 3, 4] must be understood. Insight into the properties of the spark can be gained by analyzing the voltage and current characteristics of the spark, as illustrated in Figure 1. The actual values of the current and voltage will depend on the type of discharge circuit used. Looking at these curves one can define four separate phases, a predischarge phase, a breakdown phase, an arc discharge, and a glow discharge. For a spark to occur, the predischarge and breakdown phases must exist. Then depending on the type of discharge circuit used, the spark may be terminated following the breakdown phase, or the breakdown phase can be followed by an arc or glow discharge, or both.

2.1.1 Predischarge Phase

During the predischarge or prebreakdown phase there is an initial rise in voltage on the cathode while there is no current flowing in the system. At this point, the gas volume between the electrode gap represents a

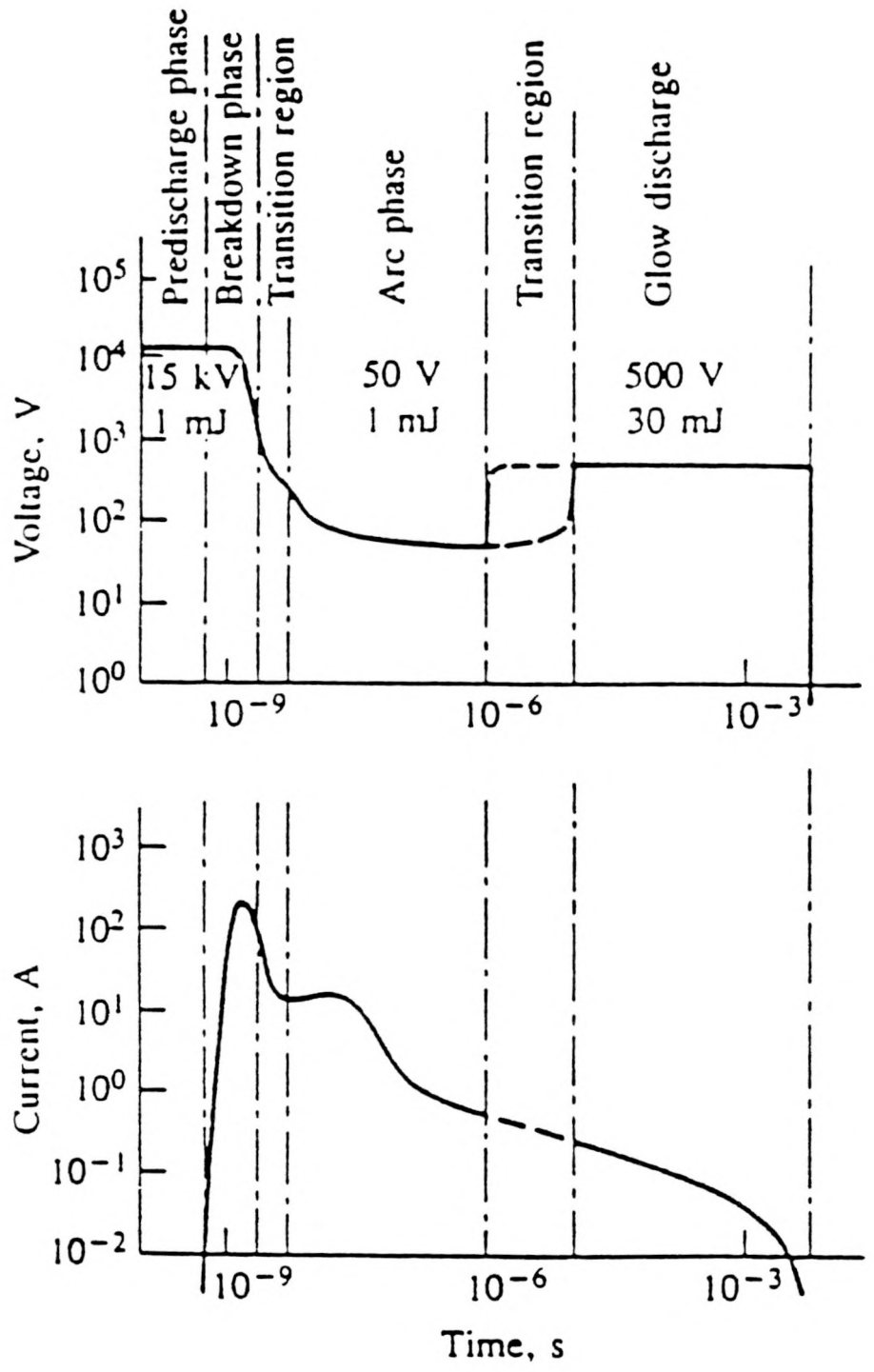

FIGURE 1: Voltage and current characteristics of the spark [3].

perfect insulator. When the spark voltage is applied, the few existing electrons in the channel between the electrodes are accelerated towards the anode. If the applied field is strong enough, the accelerated electrons may ionize gas molecules by collisions, generating additional electrons and ions, causing the number of electrons and ions to increase rapidly. However, since the electrons are collected at the anode, additional collisional processes induced by the rising cathode voltage are required to generate enough new starting electrons at the cathode to make the ionization process self-sustaining.

As long as the ionization process produces less electrons than are required for a self-sustained discharge, this process is called the prebreakdown phase. The slower the rise in ignition voltage, the longer the prebreakdown phase lasts, if pressure and gas composition are held constant. The faster the voltage rise, the shorter the prebreakdown phase due to an effective overvoltage which makes the ionization process more effective.

2.1.2 Breakdown Phase

When the cathode voltage reaches a certain critical value, V_s, enough electrons are produced and a greater than exponential increase in discharge current takes

place, creating a self-sustained spark. This process is concentrated in a narrow channel approximately 40 microns in diameter, where all the gas molecules are fully dissociated and ionized. An analytical expression can be used to solve for the voltage necessary to initiate the spark [1, p. 163].

$$V_s = bPd/\ln\{aPd/\ln(1/\tau)\} \qquad (2.1)$$

This equation is known as Paschen's Law where a and b are constants which depend on the gas, and τ is a constant representing the number of electrons emitted from a metal per impacting positive ion. Therefore, V_s is a function of the pressure P and the gap spacing d. The sparking potential for air at atmospheric pressure is [1]

$$V_s = 3.0d+1.35 \quad (kv) \qquad (2.2)$$

for a gap of the order of 1.0 mm.

In addition to the high cathode voltage, the breakdown phase is also characterized by a very high current (~100 A) and an extremely short duration, typically nanoseconds. The breakdown phase reaches the highest power levels of the three discharge phases due to the high current and voltage levels. Since this phase is extremely fast, the cathode remains cold and does not take up appreciable amounts of heat via conduction [2, p. 98]. Therefore, the energy supplied is transformed almost without loss to the plasma, where

it is stored by dissociation and ionization. An increase in breakdown energy will increase the spark channel diameter causing a larger activated gas volume. The end of the breakdown phase can be interpreted as the point when the ignition voltage has dropped below 10% of its maximum value.

2.1.3 Arc Discharge

One definition of an arc discharge is [5], "A discharge of electricity between electrodes in a gas or vapor which has a voltage drop at the cathode of the order of the minimum ionization or excitation potential of the gas or vapor."

The arc discharge must always be preceded by a breakdown phase which provides the conduction path between the electrodes. The arc discharge is characterized by currents in excess of 100 mA, very low voltages (<100 V), and durations up to hundreds of microseconds. The voltage of an arc discharge can be divided into three regions: cathode drop, positive column, and anode fall. The most important of these three regions is the cathode drop. This region is a relatively short distance in front of the cathode and accounts for a considerable amount of the arc voltage. Due to the close proximity of the cathode drop region to the electrode, a significant amount of the arc energy

can be lost via conduction back into the electrode. The cathode drop region is necessary to maintain numerous hot spots on the cathode. Without such spots of molten metal the arc cannot exist [2].

2.1.4 Glow Discharge

The third and final phase of the spark is the glow discharge. Voltages near 1 kV can be seen in this phase, however, only low currents (<100 mA) can be sustained. This phase is usually the longest and deposits the largest amounts of energy of all three phases.

In order to maintain the glow discharge for long durations (~milliseconds), a high cathode drop is needed to provide enough electrons at the cathode. In a glow discharge the cathode drop obeys the following relation [1, p. 225].

$$V_n = (3b/a)\ln(1+1/\tau) \quad \text{(volts)} \qquad (2.3)$$

Since the cathode drop region is very close to the cathode surface, a significant fraction of the energy input by the glow discharge is conducted back into the cathode. With long duration glow discharges, appreciable amounts of the input energy, up to 92%, are lost in the cathode drop region [2].

2.1.5 Energy-Transfer Efficiencies

Due to the properties of the discharge modes, only a fraction of the supplied electrical energy may be transmitted to the mixture for inflammation [2, 6]. The breakdown phase is the most efficient (~94%) due to its short duration. In this phase, the losses are attributed to conduction (~5%), and radiation effects (~1%) of the plasma to the surroundings. The efficiency of this phase is constant and independent of the velocity of the combustible media.

In the arc and glow phases, the energy-transfer efficiencies are much lower because of the larger conduction losses that occur in the cathode drop region. The glow phase is the least efficient due to the higher cathode drop voltage. The efficiencies of the phases can be as low as 35% for the arc and 8% for the glow. However, the arc and glow modes are favored by increasing flow velocity because the discharge channel is carried away from the electrodes reducing conduction heat losses. For flow velocities below 15 m/sec, efficiency increases steadily and can reach maxima of 50% for the arc and 30% for the glow. Beyond 15 m/sec, multiple discharges occur so that the energy is distributed to independent spark channels. For velocities less than 15 m/sec, the efficiency is a function of the flow velocity, as shown in Figure 2.

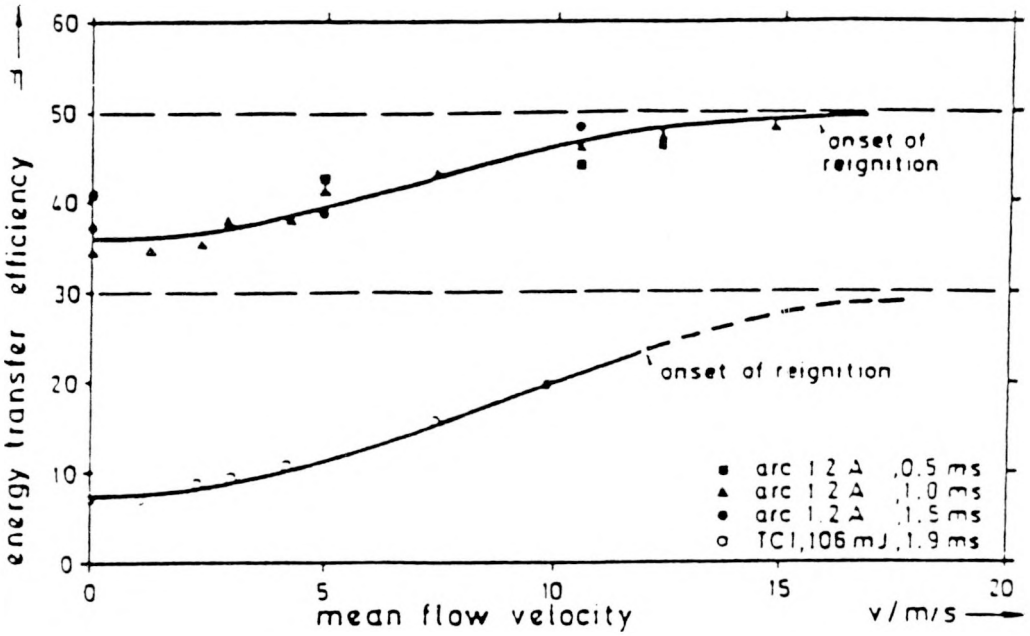

FIGURE 2: Arc and glow efficiencies as a function of the mean flow velocity [2].

2.1.6 Ignition System Energy Measurements

The most accurate way to measure the spark energy input is to measure the spark current I_g and spark gap voltage V_g [7]. The product of these two parameters is the power delivered to the electrodes, which when integrated over the spark duration yields the spark energy.

$$E = \int V_g I_g \, dt \qquad (2.4)$$

For long duration phases, this is the acceptable way to calculate the spark input energy. However, when the duration of the phase is very short, as is the case for the breakdown phase, it can be difficult to record accurate voltage and current measurements. In this case, the energy can be calculated from circuit parameters. The energy deposited in the breakdown phase can be approximated from the breakdown voltage of the plug V_s and the capacitance of the plug C_s,

$$E_b = 1/2C_sV_s^2. \qquad (2.5)$$

2.1.7 Classification of Ignition Systems

Based on the three different modes of the spark, it is possible to classify three different types of ignition systems. These three systems, arc, glow, and breakdown, are distinguished by voltage, current, and duration characteristics.

Arc discharge systems, which are preceded by a breakdown phase, have low voltages (<300 V) and high currents (>100 mA). The duration of these systems is typically less than a millisecond. Arc discharges are usually accomplished by a CD (capacitive discharge) ignition system. In a CD ignition system (Figure 3), the energy is stored in a capacitor on the primary side of a coil or pulse transformer [1, p. 93].

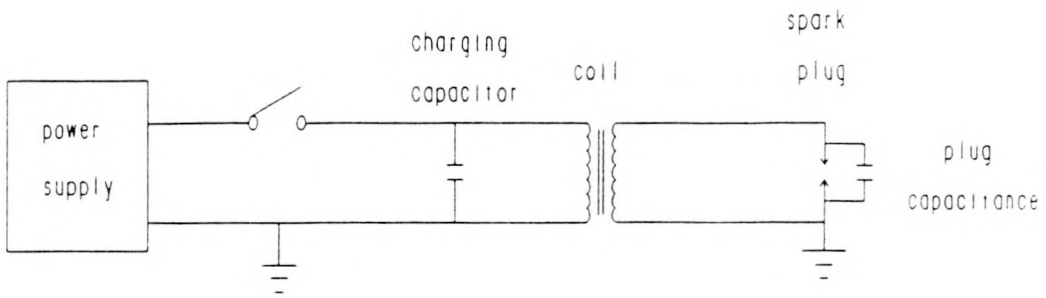

FIGURE 3: Typical CD ignition system.

This system produces a spark when the energy stored in the capacitor is first allowed to discharge through the coil or pulse transformer. The coil then causes a high voltage to be applied to the spark plug initiating the spark.

Glow systems, which are also preceded by a breakdown phase, are predominately used in automotive applications, and are characterized by long durations (~milliseconds), low currents (<100 mA), and voltages between 300-1000 volts [1, p. 104]. This type of spark can be achieved by using a standard automotive inductive ignition system. Inductive systems (Figure 4) consist of a power supply, ignition module, coil and spark plug.

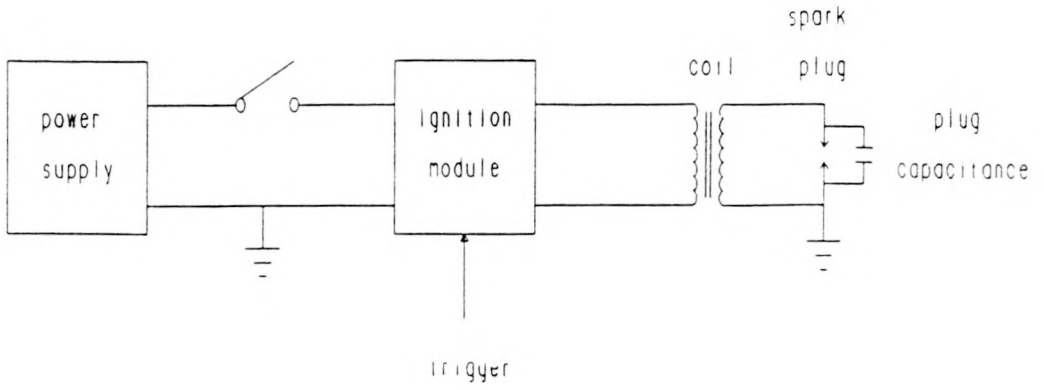

FIGURE 4: Typical inductive ignition system.

The system operates with the power supply charging the primary side of the coil. Then a trigger signal is sent to the ignition module. Once the trigger signal is received, the module shorts out the primary side of the coil, causing a high voltage rise on the secondary side. This voltage is applied to the plug and causes the spark.

Breakdown systems all have the common trait of producing short duration, high current and voltage discharges [3, 8, 9]. The main idea is to supply all the spark energy in a very short duration, typically nanoseconds, which is the characteristic duration of the breakdown phase. According to equation (2.5), the

energy of the breakdown phase can be increased by either increasing the capacitance coupled with the plug or by raising the breakdown voltage.

One type of breakdown system, which simply enhances the initial breakdown phase, consists of a spark plug that has an increased capacitance [8]. This plug differs from standard plugs by having an additional capacitance parallel to the spark plug. This results in a higher available energy for the initial breakdown.

The second type of breakdown system [3, 9] (Figure 5) consists of a basic CD ignition system along with a high voltage diode, discharge capacitor, isolation spark gap, and spark plug. High breakdown energy is achieved

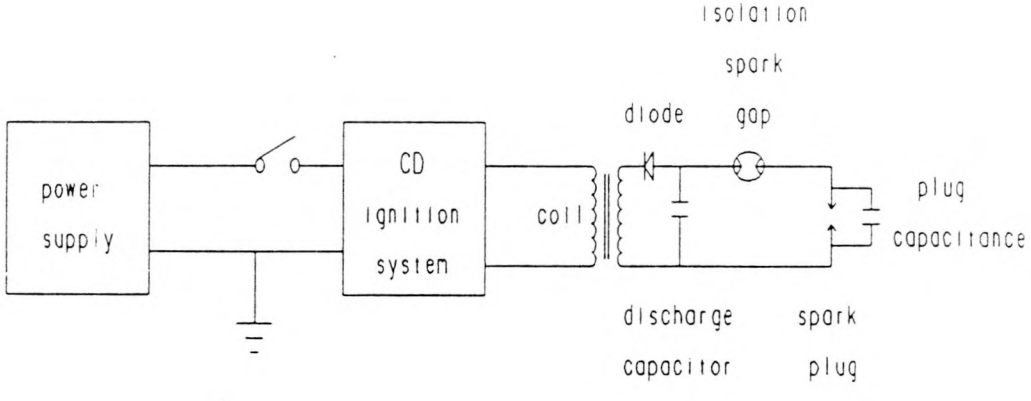

FIGURE 5: Typical breakdown ignition system.

by charging the capacitor to a specified high voltage thus increasing the breakdown voltage. This specified high voltage is determined by the static breakdown voltage, for example 20 kV, of the isolation spark gap between the capacitor and spark plug. Once the capacitor charges up to the specified voltage, the gap will start conducting, allowing the capacitor to discharge into the plug in a very short time with a high breakdown voltage. The purpose of the high voltage diode is to ensure that none of the energy stored in the capacitor discharges into the coil, and that the energy is deposited directly into the spark plug without oscillations between the coil and the capacitor.

2.2 Processes Involved in the Formation and Growth of Ignition Kernels

The formation and growth of an ignition kernel is dependent on three separate regimes. The first regime is the initial formation of the kernel, which is mainly influenced by the breakdown phase of the plasma. The second phase of kernel growth occurs simultaneously with the arc and/or glow discharge, and is referred to as the spark assisted regime. The final phase of the kernel's growth takes place following the completion of the spark and is dominated by the chemical heat release of the combustion reactions.

2.2.1 Initial Growth

The initial development of the plasma/flame kernel is primarily controlled by the breakdown phase of the spark. Initially the plasma kernel expands rapidly to balance the sudden increase in temperature and pressure within the kernel caused by the deposition of energy. During this initial phase the high power associated with gas breakdown produces a shock wave which quickly separates from the plasma kernel [3, 10].

The plasma kernel at this time has attained its maximum temperature, approximately 60,000 K, and possesses high concentrations of radical and ionized species [3]. The high concentrations and temperatures are primarily due to the high efficiency of the breakdown phase where energy losses are small. If the energy deposited in the plasma kernel is sufficient to maintain the gas temperature and radical concentrations above the critical level needed to sustain chemical reactions until the kernel reaches its critical size, a self-sustaining flame kernel will have formed and ignition will have occurred [10].

Once a flame is established, the flame kernel growth rate is in part determined by the thermal expansion required to accommodate the flame's heat release. This occurs at a rate proportional to the laminar flame speed

which depends on the diffusion of thermal energy, as well as the radical and ionized species, from the burned gas to the flame's reaction zone.

If the breakdown energy is increased, higher concentrations of chemically reactive radical and ionized species are generated. The increase in chemically reactive species results in an enhanced initial flame speed due to radical diffusion. This increase in breakdown energy does not result in higher kernel temperatures [3]; instead the initial size of the kernel increases causing a larger activated gas volume. This larger initial size results in higher temperatures and higher radical concentration possible farther from the electrodes. This increase in breakdown energy results in both a larger and more rapidly growing initial flame kernel.

In addition to diffusion processes, the initial growth is enhanced by a suction phase which follows the shock front [3]. This suction phase is caused by the inertia of the gas molecules that are projected outward due to the expansion of the spark channel. The unburnt gas then flows along the electrode surface into the gap. The influx of fresh gas creates an intense microturbulence which may further accelerate the burning rate.

Increasing breakdown energy can also alter the

effects of turbulence on ignition flame kernel growth in one of two ways [11]. If the length scale is relatively small, increasing the breakdown energy can cause the kernel to grow to a larger more stable size before the onset of significant turbulence effects. Or, if the turbulent length scale is relatively large, increasing the breakdown energy will shorten the time required for the kernel size to become large enough where turbulence effects are important. Both of these effects tend to enhance the initial growth of the flame kernel. However, if the turbulence intensity is very high, the growth rate of the kernel can be adversely affected by flame stretch effects. Also, in extreme cases, the spark itself can be quenched by stretch effects [12].

2.2.2 Spark Assisted Growth

If gas breakdown is followed by an arc and/or glow discharge, the flame kernel growth rate is also affected by the rate of energy supplied by the arc and/or glow discharge, and is referred to as spark assisted growth [2, 12]. Typically, during this period, the growth rate of the kernel is very repeatable [13, 14] and is dominated by thermal expansion [2, 12]. During this time high temperatures and radical concentrations still exist from the breakdown phase, which as discussed previously control the growth rate of the kernel.

In this region the growth of the kernel is dominated by the thermal expansion which is required to accommodate the electrical energy supplied by the discharge. Some of the electrical energy is also converted into dissociation energy; however, this energy, stored in radicals [2], is also converted into thermal energy as the radical species begin to recombine.

With the growth of the kernel depending on the nature of the spark, it would be expected that arc discharges would have greater growth rates than glow discharges. Arc discharges have higher efficiencies than glow discharges. This higher efficiency should result in more available electrical energy causing more rapid thermal expansion rates for arc discharges. Experimental evidence does support the conclusion that when equal glow and arc discharge energies are supplied in a combustible media, the kernel growth of the arc discharge is faster [3, 4, 9].

The final area of interest in this process is the effect of flame stretch. Two separate types of flame stretch can affect the growth of the kernel. Geometric flame stretch, which is directly proportional to the growth rate and inversely proportional to the kernel radius, and turbulent flame stretch. Flame stretch can either enhance or diminish flame growth, depending upon

the fuel molecular weight and the equivalence ratio of the mixture. Due to the small size of the flame kernel, observations of lean propane mixtures show the adverse effects of stretch will diminish the growth rate and could even extinguish the flame. Therefore, for lean propane mixtures in this region, the phase needs to be spark assisted to counteract the adverse effects of stretch to ensure flame propagation [12, 15].

2.2.3 Flame Front Propagation

After the period of spark assisted growth, a second transition occurs. During this time the growth of the kernel depends only on the burning rate of the propagating flame front.

An expression for the development of the flame kernel in this regime can be formulated from the continuity equation. By equating the mass flux in front of the flame to that behind the flame, an expression for the expansion of the kernel can be obtained.

$$\rho_u A S_l = \rho_b A (dr/dt) \qquad (2.6)$$

$$dr/dt = (\rho_u/\rho_b) S_l \qquad (2.7)$$

Where S_l is the laminar flame speed, A the surface area of the flame kernel, and the subscripts u and b refer to the unburnt and burnt gases, respectively. It is assumed that the flame propagates radially. In this regime the boundary of the kernel grows at a subsonic

rate, therefore a pressure gradient cannot exist across the boundary [16], and the pressure can be assumed constant if the kernel is free to expand. If the mixture also behaves as a perfect gas, an alternate expression can be formulated using the perfect gas law.

$$P = \rho RT \tag{2.8}$$

$$dr/dt = (T_b/T_u)S_l \tag{2.9}$$

Expressions (2.7) and (2.9) define what is known as the laminar expansion of the flame kernel. It is a result of flame propagation through the unburnt gas, along with gas expansion as it is heated from T_u to T_b [13].

The laminar expansion expression, in terms of either the temperature or density ratio, has been shown to be applicable in many combustion environments. In an engine with mild turbulence levels, a laminar-like burning process was shown to immediately follow the spark discharge [8, 17]. These results were in good agreement with equation (2.7). In a flow reactor under flowing and stagnation conditions it was observed that for flammable mixtures the steady state growth corresponds to the establishment of a constant expansion of the form of equation (2.9) [18]. Other experiments conducted in combustion bombs [16, 19, 20] also show the regime of laminar expansion. Champion et. al. [20] noticed this region when the flame radius was beyond an

unstable radius. The unstable radius was defined as a critical radius where if the kernel reached this size it spontaneously expanded into a flame. If the kernel did not reach the unstable radius, the kernel collapsed and was quenched. For the case of propagating kernels, the growth rate reaches the laminar expansion regime immediately after the kernel grows to a size larger than the unstable radius.

2.2.3.1 Effects of Equivalence Ratio

The variation of the laminar expansion rate with changes in the equivalence ratio are manifested through changes in the flame temperature and flame speed. These two parameters are coupled since the laminar flame speed is a function of the flame temperature.

For hydrocarbon fuels the maximum flame temperature and flame speed occur in stoichiometric or slightly fuel rich mixtures. The primary reason for this is that on the lean side the reaction is slowed due to a lack of fuel, and on the rich side by a lack of oxygen. Both of these factors decrease the flame temperature and flame speed. It is generally acceptable to assume that a mixture with maximum flame temperature is also a mixture with maximum flame speed [21, p. 313].

The variation of flame speed with equivalence ratio was studied for methane mixtures [13] and for propane

mixtures [22]. For methane mixtures the equivalence ratio was varied from 0.7 to 1.3 and it was found that the maximum flame speed occurred at the stoichiometric condition. The equivalence ratio in the propane tests varied between 0.8 and 1.5, with the maximum flame speed occurring near an equivalence ratio of 1.1.

Therefore, in the laminar expansion growth period, increasing the equivalence ratio of lean mixtures and decreasing the equivalence ratio of rich mixtures, to the point of maximum flame temperature, will increase the laminar expansion by increasing the unburnt gas temperature T_b and the laminar flame speed S_l.

2.2.3.2 Effects of Dilution

As with equivalence ratio, changes in the laminar expansion due to dilution are the result of changes in the flame temperature and flame speed. Combustion bomb experiments using various fuels were conducted with nitrogen dilution levels of 15% CO_2 by volume [23]. All of the fuels showed the same trend of decreasing laminar flame speed with increasing mass diluent. On average, a 27% reduction in flame speed was seen with each 10% increase in mass of the diluent.

Other experiments also studied the effects of dilution on flame speed and temperature for various fuels and diluents [24]. The diluents used in these

experiments were argon, helium, and nitrogen. The experiments showed that the presence of the diluent caused both the flame temperature and speed to decrease. At a given percent dilution, the flame speed and temperature of the nitrogen mixture were the lowest, followed by argon, then helium. These differences can be explained by considering the thermal diffusivity and specific heat of the diluents [21, p. 314].

Helium and argon are both monatomic gases with the same specific heat. However, the flame speed with helium dilution is larger than with argon due to helium's higher thermal diffusivity. Argon and nitrogen have nearly the same value of thermal diffusivity. For these two gases, the difference lies in the specific heats, with argon, a monatomic gas, having a lower specific heat, $C_p=(5/2)R$, than diatomic nitrogen, which has a minimum specific heat of $C_p=(9/2)R$. For a system with the same percent dilution, the heat release will be the same. However, the flame temperature for the case of argon dilution will be greater than with nitrogen dilution, due to its lower specific heat, causing a higher flame speed.

2.2.3.3 Effects of Pressure

The effects of pressure on the laminar expansion of the flame kernel are also seen through changes in the

laminar flame speed. Two laminar flame theories--the thermal theory of Mallard and LeChatelier based on energy considerations and the comprehensive theory of Zel'dovich, Frank-Kamenetsky, and Semonov which considers both energy and species influences--predict the following pressure dependence on laminar flame speed:

$$S_l \propto P^{(n-2)/2}, \tag{2.10}$$

where n is the order of the reaction [21].

In light of the power law prediction of the theory, experiments have been conducted to quantify the variation of flame speed with pressure [22, 25, 21, p. 312]. Propane was used as the test fuel in one set of experiments, and the initial temperature, as well as, pressure was varied [22]. The collected data were fit to a power law of the form

$$S_l = S_{lo}(T_u/T_{uo})^{\alpha}(P/P_o)^{\beta} \tag{2.11}$$

where P_o=1 atm and T_{uo}=298 K. The value of S_{lo} is a reference flame speed which depends on mixture composition, and α and β are fitted constants. The laminar flame speed of propane, at fixed temperature, was observed to decrease with increasing initial pressure, and a value of -0.2 was obtained for β. This same approach was also used to evaluate the effects of different fuels [25]. These results also showed S_l decreasing with increasing pressure, where the exponent

varied between -0.33 to -0.5 for the different fuels.

One other experiment also studied the effect of pressure on the flame speed for different fuels [21, p. 312]. Observations showed that for fuels with S_l < 50 cm/sec the laminar flame speed decreased with increasing pressures. However, for fuels with flame speeds between 50 cm/sec and 100 cm/sec, S_l was independent of pressure, and when S_l > 100 cm/sec flame speed increased with increasing pressure. These results are in good agreement with theory, in that for fuels with S_l < 50 cm/sec the reaction order n is less than two, for fuels with 50 cm/sec < S_l < 100 cm/sec, n=2, and for fuels with S_l > 100 cm/sec the reaction order is greater than 2. Experimental evidence does support the relationship between pressure and reaction order. Tests show that for first order reactions, S_l is inversely proportional to pressure, and that for many hydrocarbon fuels undergoing second order reactions, S_l was found to be pressure independent [21, p. 313].

Therefore the effects of pressure on the laminar expansion of the flame kernel can either increase or decrease with increasing pressure, depending on the reaction order of the mixture.

2.2.3.4 Effects of Initial Temperature

Initially, upon evaluating equation (2.9) it would be expected that the laminar expansion would decrease as the initial temperature increases. However, the role of initial temperature on flame speed and flame temperature must be considered.

According to equation (2.11) the laminar flame speed could increase or decrease with initial temperature depending on the value of the constant α, if pressure is held constant. The value of α was found to be approximately 2 for propane [22]. Thus the laminar flame speed of propane increases with increasing initial temperature.

Similar experiments were performed for various fuels [21, p. 313], where the relationship used to fit this data was

$$S_l \propto T_u^m, \qquad (2.12)$$

where m varied between 1.5 and 2 for the various fuels. Also, since the flame speed and flame temperature are directly related, increases of the flame speed with initial temperature also must increase the flame temperature T_b.

Referring back to equation (2.11), the laminar expansion should increase with initial temperature since the increase in flame speed and flame temperature will be greater than the increase in initial temperature.

2.2.3.5 Effects of Fuel Type

The maximum laminar flame speeds for hydrocarbon fuels fall in the order of alkynes > alkenes > alkanes [26]. For the alkane fuels, $S_{l_{max}}$ is nearly independent of the number of carbon atoms in the fuel molecule. However, for the alkene and alkyne fuels the laminar flame speed decreases as the number of carbon atoms increase. The value of $S_{l_{max}}$ falls steeply as the number of carbon atoms increase to four, and then falls slowly with further increase in carbon atoms, and approaches the value of the alkane fuels when the number of carbon atoms is greater than or equal to eight [27]. The reason for these differences in the alkenes and alkynes arises from the variations in thermal diffusivity between the fuels. Fuels with smaller molecular weights have higher diffusivities, while larger fuel structures have lower diffusivities [21, p. 310]. Thus as before, the laminar expansion rate will either increase or decrease depending on whether the flame speed increases or decreases.

2.2.3.6 Effects of Turbulence

The effects of turbulence on flame speed are much the same in an ignition kernel as in a fully developed turbulent flame. Depending on the size of the flame

kernel, three different turbulence length scales can affect the kernel [10, 11, 12, 15, 28].

The length scales which are smaller than the flame thickness increase the transport rates within the flame and increase the local burning rate. When the turbulence length scales are larger than the flame thickness and smaller than the kernel diameter, they act to wrinkle and distort the surface of the kernel. This wrinkling increases the flame kernel's surface area and results in an increase in the burning rate. Turbulence scales which are larger than the flame kernel act to convectively displace the entire ignition kernel, leading to cycle to cycle variations [11]. Therefore, the effect of turbulence changes with time as the size of the flame kernel changes relative to the distribution of turbulence length scales.

To account for the effect of turbulence on the flame kernel growth rate, one can simply replace the laminar flame speed in equations (2.7) and (2.9) with a turbulent flame speed.

$$dr/dt = (\rho_u/\rho_b)S_T(t) \qquad (2.13)$$

$$dr/dt = (T_b/T_u)S_T(t) \qquad (2.14)$$

The turbulent flame speed is a function of time since as the kernel grows it is affected differently by the different turbulence length scales present.

2.2.3.7 Effects of Stretch

The initial rapid increase of the ignition kernel surface gives rise to what is referred to as geometric flame stretch [12, 15, 29]. Flame stretch is caused by flow nonuniformity, flame front movement, and flame curvature, and can either diminish or enhance the kernel growth depending on the conditions present.

A general definition of the geometric stretch rate is the time derivative of the infinitesimal flame area element.

$$K = (1/A)\,dA/dt \qquad (2.15)$$

This expression can also be written in terms of the flow variables,

$$K = \{\nabla_t \bullet v_t + (V \bullet n)(\nabla \bullet n)\}_s \qquad (2.16)$$

where ∇_t and v_t are the tangential components of the gradient operator, ∇, and the fluid velocity, v, at the flame surface, with n the unit outward normal vector, and V the flame surface velocity. The stretch rate, K, has units of 1/sec. The first term in equation (2.16) shows the influence of stretch due to flow nonuniformity along the surface and flame curvature. The second term represents stretch experienced by a nonstationary flame. By definition $K > 0$ for positively stretched flames and $K < 0$ for negatively stretched or compressed flames.

The influence of stretch on flame response can be divided into two regions, at the flame, and in the transport zone ahead of the flame. In these regions the tangential and normal velocity components have different effects on stretch. At the flame front, the tangential velocity gradient changes the flame area and corresponding burning rate. Positive stretch increases the burning rate while negative stretch decreases it. The normal velocity gradient at the flame front acts to adjust the flame position to where the flame speed balances the local normal velocity. Therefore, at the flame the velocity gradients cause surface displacement, flame distortion, and changes in burning rate.

In the transport zone, the tangential velocity gradient affects the normal mass flux entering the reaction zone, along with the heat flux and species diffusion processes across the flame surface boundary. This causes changes in flame temperature and species concentrations. The normal velocity gradient in this region affects the residence time within the zone and consequently flame temperature and completeness of reaction. These two effects are collectively known as flame stretch.

The effects of flame stretch on kernel growth are seen through changes in the flame temperature which correspondingly affects flame speed. In the case of

nonadiabatic flame kernels, heat losses lower flame temperatures and burning rates, and the influence of stretch is coupled with heat loss. Stretching changes the proximity of the kernel to the heat sink, and flame curvature changes the intensity of heat flux over the flame surface. These two coupled stretch mechanisms, associated with non-adiabatic kernels, can diminish the growth of the kernel, and can cause extinction if enough heat is transferred away from the kernel.

In diffusionally imbalanced mixtures, the effects of flame stretch on flame temperature differ depending on whether the Lewis number of the mixture is greater than or less than one. For Le > 1, flame kernel heat loss exceeds mass gain causing the flame temperature to be less than the adiabatic flame temperature with stretch effects present. The converse is true for Le < 1 mixtures. Due to diffusional effects, for Le > 1 mixtures, an increase in the stretch rate will lower the flame temperature until extinction occurs from incomplete reaction. However, for Le < 1 kernels, increasing stretch increases the flame temperature and extinction can only occur through other quenching mechanisms.

If the differential diffusion of reactants is considered, the above phenomenon can be explained. When the leaner reactant is more diffusive, the reactant

concentration at the flame front will become closer to stoichiometric as stretch increases, and will increase flame temperature. The converse is true if the leaner reactant is less diffusive.

Experimental results support these conclusions [29]. For lean methane and rich propane flames, whose effective Lewis numbers are less than one, flame temperature increases with increasing stretch. However, for rich methane and lean propane (Le > 1) flame temperature decreases with increasing stretch. The effective Lewis numbers are based on the diffusivities of the reactants with respect to nitrogen, and increase in the order of propane, oxygen and methane. Thus for positive stretch methane concentration will increase and propane decrease at the flame. This positive stretch makes lean methane and rich propane flames move closer to stoichiometric at the flame front, and rich methane and lean propane flames move away from stoichiometric conditions at the flame.

For ignition flame kernels, if the kernel is approximated as a sphere, the stretch rate is

$$K = (2/r)\, dr/dt \qquad (2.17)$$

and is positive. Therefore, when the ignition kernel is small the effects of stretch are very high.

In addition to geometric flame stretch, a turbulent flame stretch can also be defined [12]. Here stretch is

related to the residence time of the reactants in the flame front, represented nondimensionally by the inverse Damkohler number, which is the ratio of the chemical lifetime divided by the eddy lifetime. If the characteristic eddy lifetime is exceeded by the chemical lifetime flame quenching can occur. The turbulent flame stretch rate can be define as

$$K = u'/\lambda_T \qquad (2.18)$$

where u' and λ_T are the turbulence intensity and Taylor microscale respectively. As K increases, the kernel becomes severely folded with partial quenching of the reaction in some regions, and eventually extinction can occur.

For turbulent flame initiation, it is assumed that the geometric and turbulent stretch rates are additive.

$$K = u'/\lambda_T + (1/A)dA/dt \qquad (2.18)$$

Although an initial increase in u' will usually lead to favorable effects on kernel growth, significant increases in the turbulent intensity may diminish kernel growth through adverse stretch effects.

The presence of stretch in spark ignited flame kernels can influence kernel growth in three ways. First, since spark kernels are non-adiabatic, due to heat losses to the electrodes and usually a wall surface, stretch tends to decrease kernel growth. Secondly the effects of geometric stretch can either

enhance or diminish growth depending upon the mixture Lewis number. Finally, the effects of turbulent stretch tend to diminish growth due to reaction quenching.

Chapter 3

EXPERIMENTAL DESCRIPTION

3.1 Turbulent Flow Reactor

The turbulent flow reactor shown in Figure 6 was used to simulate idle conditions. The flow reactor consists of three separate gas delivery systems. The first delivery system supplies air via a compressor and storage tank regulated to 80 psi. The flow rate of the air is controlled by a metering valve and monitored on a rotameter. The second delivery system is for the propane fuel. The fuel rate is recorded by a digital flow meter (Hastings model nall-P) and regulated by a metering valve. The fuel supplied to the system can be turned on or off manually by a toggle switch operating a solenoid valve. The final delivery system is for the nitrogen diluent. All gases from the three delivery systems are combined well upstream of the test section to ensure complete mixing of the charge.

Turbulence is generated by first passing the mixture through a slit plate. This plate consists of either one or two .8 mm wide slots designed to produce flow with large scale turbulent structures. These structures then pass through a converging section designed to breakup

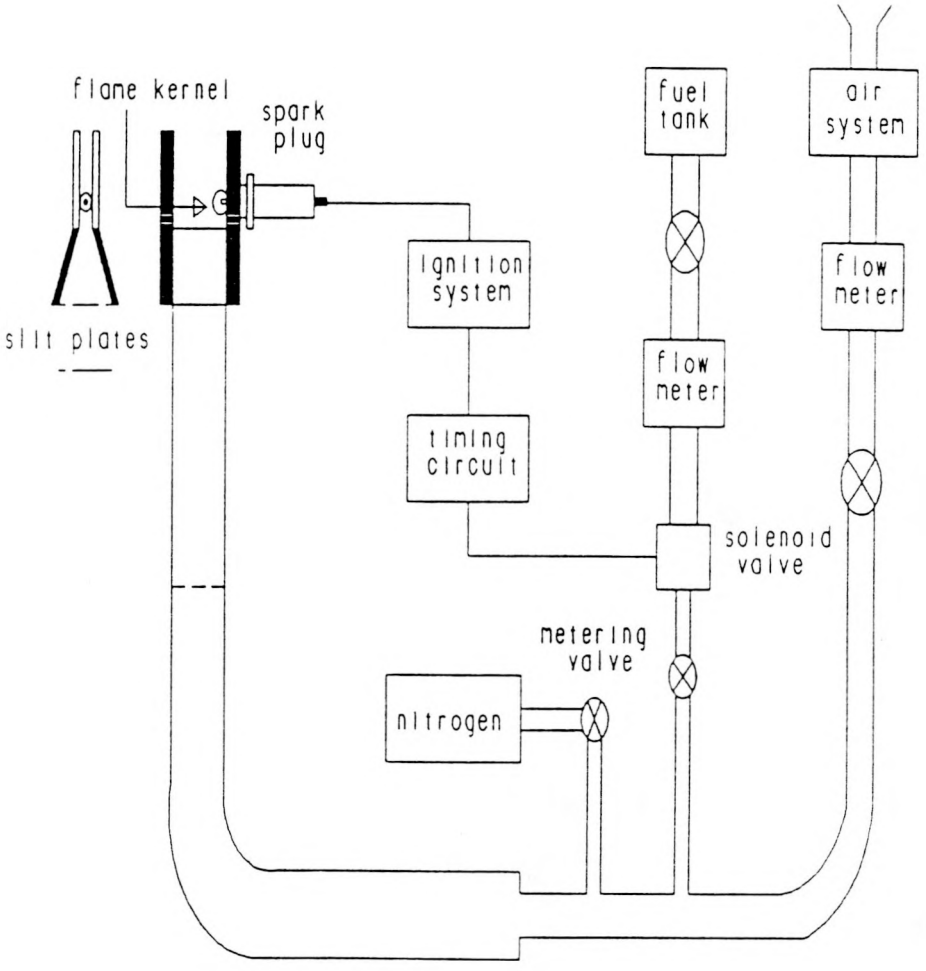

FIGURE 6: Turbulent flow reactor.

the large scale eddies before they enter the test section.

The actual test section is 13 mm by 64 mm in cross section. The 64 mm wide walls are made of quartz to provide optical access for shadowgraph measurements. On one of the 13 mm walls a non-resistive J-gap spark plug (Champion Z-8) is mounted to provide the spark. The test section geometry is representative of a "pancake"-shaped combustion chamber with side wall ignition.

The timing electronics for this experiment consist of a toggle switch to control the fuel solenoid valve along with a momentary switch to activate the spark. The electronics, which are described in Appendix A, were designed to operate the ignition systems in a single spark mode. Single spark operation is accomplished by a trigger signal sent to the ignition relay. The trigger signal is a 5 msec long TTL pulse.

The electronics system provided three separate output pulses. The first output signal is sent as soon as the momentary switch is released. The second and third signals are delayed with respect to the first signal. Delay times of up to 12 msec can be achieved. The first output signal is usually sent to trigger the ignition system while one of the remaining two enables an A/D converter to record the electrical characteristics of the spark.

3.2 Ignition Systems

Three different ignition systems were used to study early flame kernel growth. These ignition systems were all based on the production version of the General Motors high energy ignition (HEI) system [30]. The three systems used were the standard HEI, a capacitive HEI, and an enhanced breakdown HEI.

3.2.1 Standard HEI

The standard GM HEI, as illustrated in Figure 7, is a glow or inductive system consisting of a power supply (15 volt, 6 amp), GM ignition module (#1875990), GM coil (#1115455), and a spark plug. To operate this system the TTL trigger pulse is first supplied to the ignition module. Upon receiving the trigger signal the module shorts out the primary side of the coil which is storing energy, causing a high voltage rise on the secondary side. The secondary voltage is applied to the spark gap and initiates the spark.

3.2.2 Capacitive HEI

The second type of ignition system used was a capacitive HEI, as illustrated in Figure 8. In addition to the base HEI system, a capacitance of 6100 pf was placed in parallel with the spark gap. A high voltage

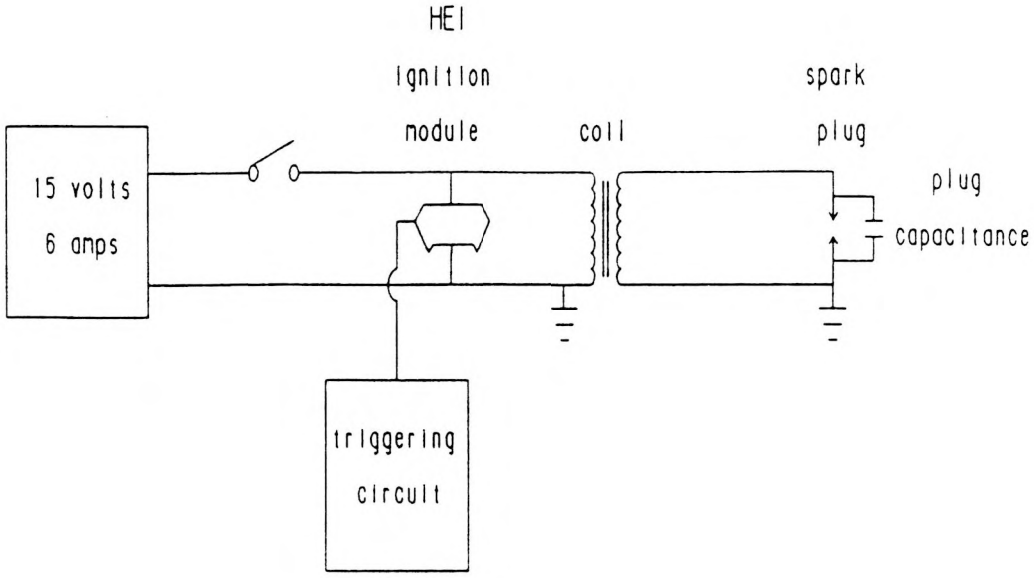

FIGURE 7: Standard HEI ignition system.

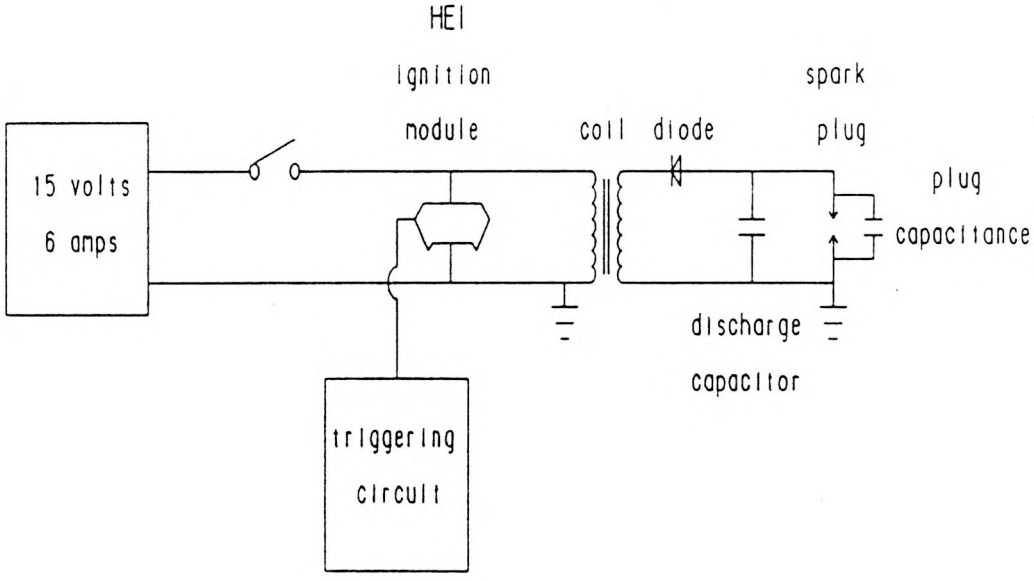

FIGURE 8: Capacitive HEI ignition system.

diode (CSDC 45XV804) was also added between the coil and capacitor. The operation of this system follows that of the standard HEI, except that the high voltage on the secondary side of the coil charges both the plug and the added capacitors, which then discharge into the spark plug. The purpose of the diode is to insure that when the capacitors discharge the current flows directly into the plug without oscillations to the coil. This system provides the same amount of energy to the plug as the standard HEI, assuming no losses between the coil and capacitance. However, the power levels of this spark are higher and the duration shorter.

3.2.3 Breakdown HEI

The final ignition system used in this study was an enhanced breakdown HEI, illustrated in Figure 9. The standard HEI system and the high voltage diode are used along with a 20 kV isolation spark gap (EG&G OGP-44G-20) placed in series with the spark plug. The nature of the isolation spark gap is such that it will consistently charge to a voltage of 20 kV, before allowing current to flow to the plug. Since the voltage applied to the plug at breakdown will be 20 kV the energy deposited in the breakdown phase is substantially increased. Again, assuming no losses in the system, the remainder of the energy will be deposited in a glow discharge. This

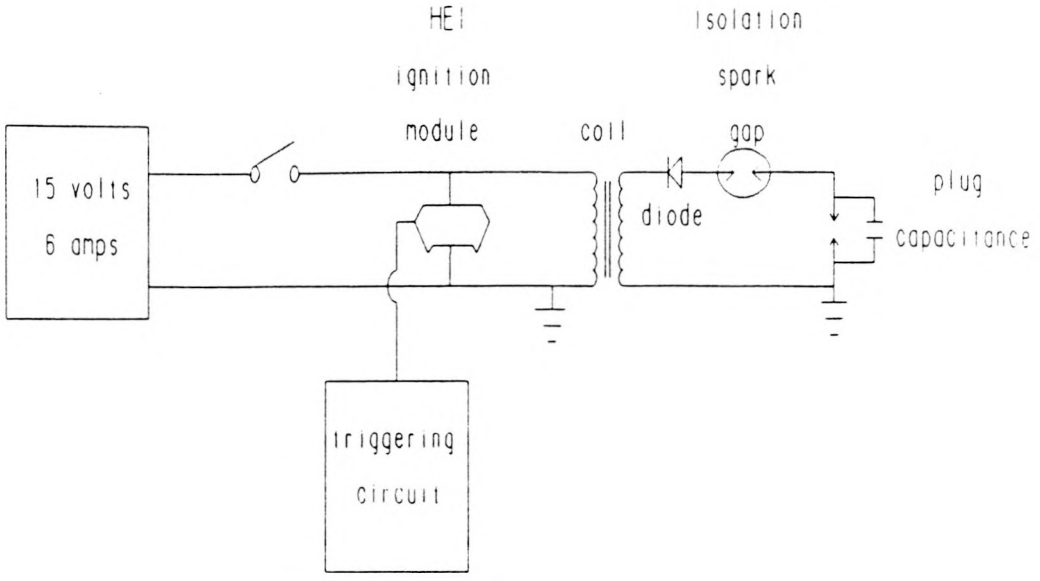

FIGURE 9: Breakdown HEI ignition system.

system, due to the high breakdown voltage, possesses the highest power levels of all three systems.

3.3 Shadowgraphy

In addition to the ignition system measurements, another principle variable of concern is the evolution of the flame kernel radius with time. The method used to record the kernel radius is a direct laser shadowgraph technique.

The shadowgraph method is a commonly used technique for flow visualization. This technique is well suited for combustion environments due to its sensitivity to

changes in the second derivative of density. For flames, the density gradients at the flame front are sufficiently high to give good contrast in the shadowgraph image [31].

The physical phenomenon behind the shadowgraph technique is light refraction. When parallel light is passed through a medium which has density changes the light will be bent an angle ϵ due to changes in the refractive index, n. The refractive index, n, is related to the density by

$$n-1 = (n_o-1)\rho/\rho_o \qquad (3.1)$$

where n_o and ρ_o are the refractive index and density at a reference temperature and pressure. For regions of higher density within the flow the light will be deflected inward toward the kernel's center at an angle ϵ_y. This angular deflection is related to the refractive index by

$$\epsilon_y = 1/n_o \int_0^{\Lambda} (\partial n/\partial y)\, dz \qquad (3.2)$$

where Λ is the path length through the test section in the direction z of the incident light.

The change in light intensity ΔI for a differential area element dxdy at the image plane a distance λ from the test section can be shown to be

$$\Delta I/I = -\lambda(\partial\epsilon_x/\partial x + \partial\epsilon_y/\partial y) \qquad (3.3)$$

$$\Delta I/I = -\lambda/n_o \int_0^{\wedge} (\partial^2 n/\partial x^2 + \partial^2 n/\partial y^2)\, dz \quad (3.4)$$

where I is the incident intensity. The ratio $\Delta I/I$ is a measure of the sensitivity of the shadowgraph image.

As mentioned earlier, the technique used in this experiment is the direct shadowgraph method, which is illustrated in Figure 10. The system utilizes a continuous wave argon-ion laser beam (Lexel model 95) for illumination. The beam is reflected off two mirrors into a lens-aperture combination which serves as a spatial filter. The spatial filter improves the spatial coherence of the laser beam and as a result the uniformity of the laser beam's Gaussian intensity profile. The expanding beam is then recollimated by a second lens placed a focal length away from the spatial filter. This lens produces a parallel light beam which illuminates the test section. The second lens also has a 55 mm aperture, giving a linear dimension to the field of view. This light is passed through the test section, illuminating the spark electrodes and creating a semicircular field of view which is 55 mm in diameter. Upon exiting the test section, the collimated light passes through a third lens which reduces the size of the shadowgraph image to match that of the photodiode of a high speed video camera. The high speed video camera (Kodak Spin Physics SP2000) records the growth of the

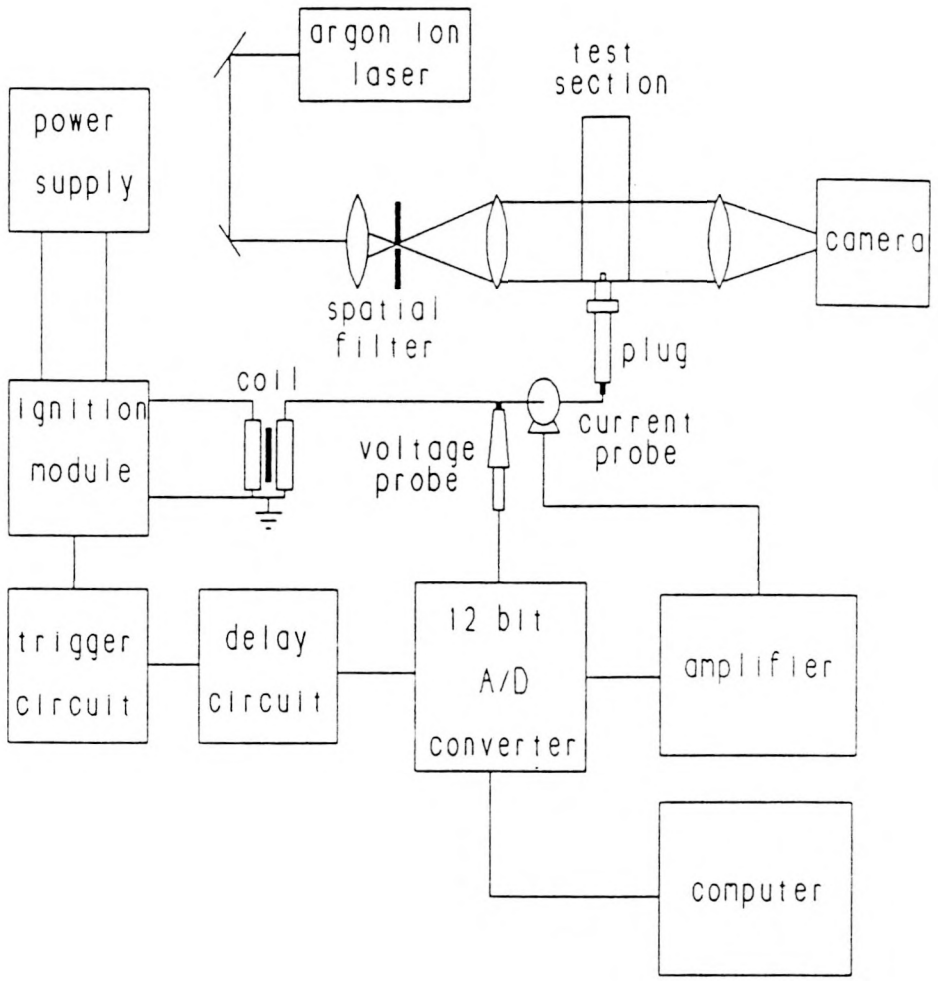

FIGURE 10: Shadowgraph and ignition energy measurement techniques.

flame kernel while operating at 4000 frames per second in the split screen mode, resulting in a time interval of .25 msec between frames.

3.4 Measurement Techniques

3.4.1 Ignition Energy

Two different types of ignition energy measurements were used, one to calculate the breakdown energy, and one to evaluate the energy deposited in the glow phase. The breakdown energy of the three ignition systems was calculated directed from equation (2.5).

$$E_b = 1/2\ C_s V_s^2 \qquad (2.5)$$

The capacitance of the plug C_s was directly measured with a capacitance meter (Precision model 820). The breakdown voltage of the spark was measured for the standard and capacitive HEI discharges with a 1000:1 divide down voltage probe (Tektronix P6015) along with a high speed 100 MHz analog storage oscilloscope (Tektronix 7623A). For the breakdown HEI system, the spark breakdown voltage was assumed to be that of the isolation spark gap, 20 kV.

The ignition energy measurements of the glow phase of the standard HEI and capacitive HEI were accomplished by digitizing the voltage and current waveforms of the spark (Figure 10). The current was monitored with a

passive current probe (Pearson Electronics model 3464), and amplified. The voltage of the spark was again measured with the high voltage probe. The current and voltage signals were fed into a computer (IBM XT) equipped with a 12 bit analog to digital board (Tecmar Labmaster) which sampled each signal at 15 kHz. The power of the spark was then obtained by multiplying the voltage and current signals together. The energy of the glow or arc phases was then calculated using equation (2.4)

$$E = \int VI \, dt \qquad (2.4)$$

by numerically integrating the power of the spark over its duration. These measurements were not possible with the breakdown HEI system due to the inadequate frequency response of the analog to digital converter.

3.4.2 Kernel Radius

Due to the uncertainties in determining time zero, the first shadowgraph image of the kernel was estimated to occur at .125 msec after the spark, which is half the time interval between successive frames. This choice was made for two reasons. First, for the standard HEI and capacitive HEI no visible light from the spark was seen on the shadowgraph, so the exact ignition time could not be determined. However, each operating

condition consisted of a set of 10 separate cases. Therefore, the average of the 10 cases should occur one-half of a frame before the frame with the first kernel. For the breakdown ignition system, visible light was seen due to the spark. However, due to the high power of this spark the shadowgraph images were distorted making it difficult to analyze the first kernel. Therefore, to maintain consistency with the other ignition cases, the same procedure for defining the time of the first kernel was adopted.

Once the image containing the first kernel was located, 35 mm slides of successive images displayed on the Spin-Physics monitor were taken. Slides of the individual flame kernels were taken until the kernel grew to a size outside of the field of view or until 8 msec had elapsed following flame initiation.

The slides of the kernel images were then projected onto a transparent table and the flame kernel boundary was digitized. The kernel boundary was digitized using an X-Y recorder (Graf/Bar Mark II) whose coordinates were stored in a computer (IBM XT). A scale factor was defined with respect to the 55 mm field of view. Knowing the scale factor, along with the X-Y boundary of the kernel, the projected area of the shadowgraph kernel was determined. With the projected area of the kernel known, an average equivalent radius was defined to be

that of half of a cylinder which possessed the same projected area, as illustrated in Figure 11.

This process was repeated 10 times for each operating condition producing 10 separate growth rate curves. These 10 curves were averaged together yielding an average growth rate curve and kernel radius standard deviation for each operating condition.

3.4.3 Turbulence Properties

The characteristic mean velocity and turbulence intensity were measured with a dual beam laser Doppler velocimetry technique. A three-dimensional flow field map of the test section was taken with the mean flow and turbulence intensity defined at each point in the map for both flow conditions.

The values reported for the mean flow and turbulence intensity were spatially averaged values of 11 points within the field of view of the shadowgraph. For the low turbulence case, the mean velocity of 1.25 m/sec varied by ±5% over the field of view, while the turbulence intensity of .30 m/sec varied by ±4%. For the high turbulence case, the mean was also 1.25 m/sec with a variation of ±25%, while the .96 m/sec turbulence intensity varied ±17% over the field of view.

The velocity profile for the low turbulence case shows uniformity over the field of view of the

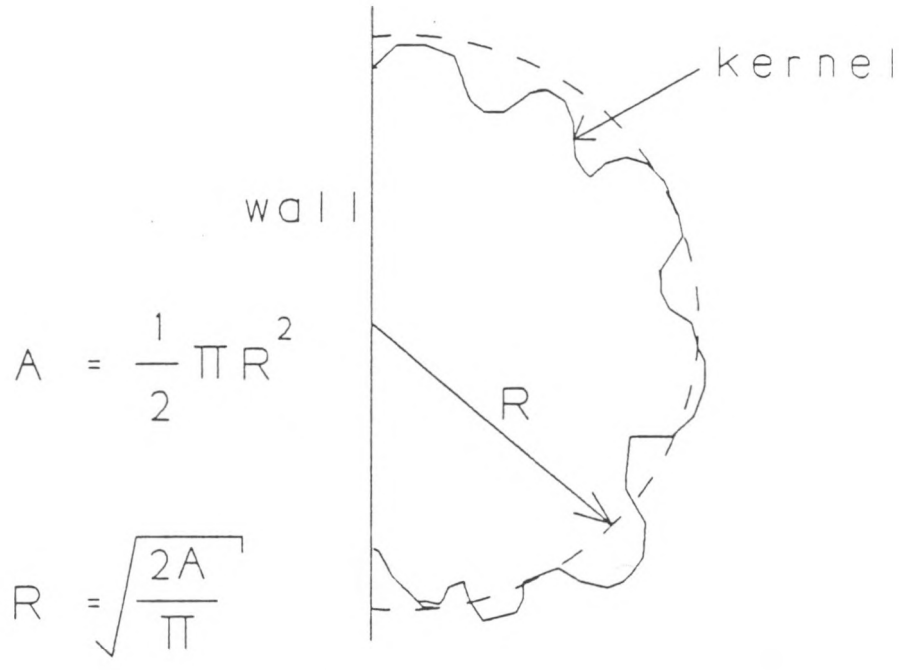

FIGURE 11: Cylindrical approximation of the flame kernel.

shadowgraph (Figure 12). For this case, the mean velocity does rise slightly as the wall is approached from the center of the test section. However, the turbulence intensity over the same distance is very flat and uniform, which was typical for the low turbulence case.

The velocity profile over which the greatest variation occurred was radially outward from the plug into the center of the test section for the high turbulence case (Figure 13). Here the mean flow decreased then increased, while the turbulence intensity rose slightly as the wall was approached. However, this profile showed the most non-uniformity for this flow condition. All other velocity profiles measurements taken for this case were predominately uniform with variations in the mean flow and turbulence intensity of approximately ±14% and ±11%, respectively, over the entire field of view.

The length scale was not measured but assumed to be equal to approximately one-fourth of the smallest test section dimension, based on analogy to the length scale at top dead center in an engine. Therefore, the integral length scale was assumed to be 3 mm.

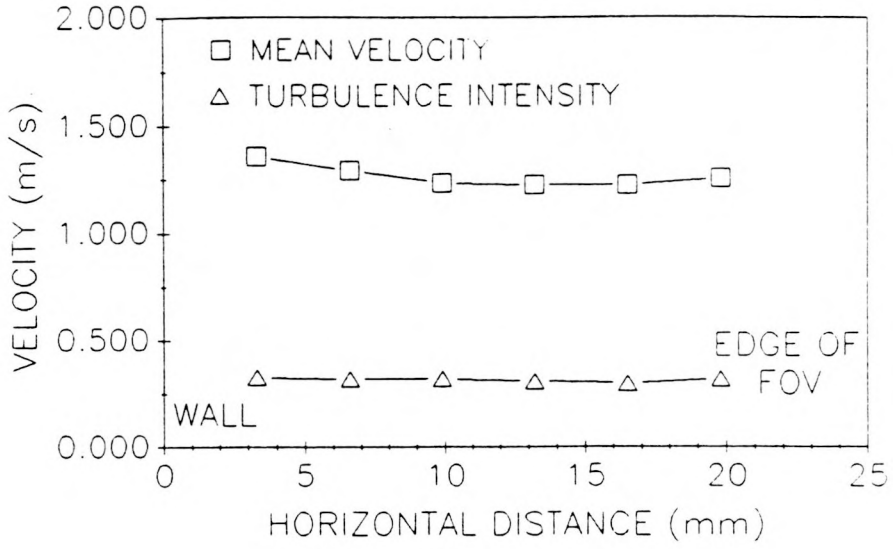

FIGURE 12: Velocity profile for the low turbulence flow condition.

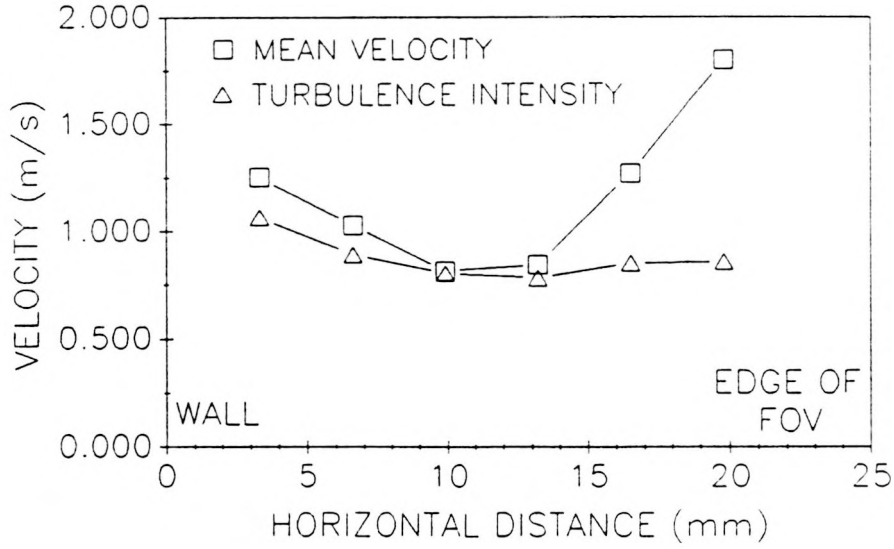

FIGURE 13: Velocity profile for the high turbulence flow condition.

Chapter 4

RESULTS AND DISCUSSION

4.1 Operating Conditions

The operating conditions used in this experiment are shown in Table 1. The goal was to match the conditions present at idle operation. At idle operation, ignition timing can be advanced as much as 30 degrees BTDC,

Table I: Operating Conditions

Pressure	1 atm
Temperature	300 K
Fuel	Propane
Equivalence Ratio	1.0
Diluent	Nitrogen
% Dilution	0% & 15%
Mean Flow	1.25 m/s
Turbulence Length Scale	~ 3 mm
Turbulence Intensity	.30 m/s & .96 m/s
Spark Plug Gap	1.2 mm
Ignition Systems	Standard HEI
	Capacitive HEI
	Enhanced Breakdown HEI

reducing cylinder pressure and temperature to 2 atmospheres and 500 K respectively at the time of ignition. These idle conditions were simulated using a pressure of 1 atmosphere and a temperature of 300 K. Propane fuel was used with an equivalence ratio of 1.0.

The choice of propane was based on its chemical structure, which is similar to the fuels used in spark ignition engines. The equivalence ratio of 1.0 was used to match the equivalence ratio present at idle. The diluent was nitrogen, where two dilution cases, i.e. 0% and 15%, were used.

The mean flow velocity of 1.25 m/sec, and length scale of approximately 3 mm were chosen to match engine idle conditions, where comparable mean flows and length scales have been measured [33, 34]. The length scale in the flow reactor was assumed to be approximately 3 mm based on analogy to engine measurements where the length scale is a fraction, e.g. one-quarter, of the clearance height. Two separate turbulence intensities of .30 m/sec and .96 m/sec were used to characterize the effects of turbulence on flame kernel growth. Again these values were chosen to be representative of the turbulence conditions measured in engines at idle speeds [33].

The spark plug gap in the experiment was held constant at 1.2 mm. Three different ignition systems were used, all based on the General Motors high energy ignition system (HEI). The first system was a standard HEI, which is an inductive type discharge, and deposits the majority of its energy in the glow phase. The second system was a capacitive discharge HEI, which was

also classified as a glow discharge. The final system used was an enhanced breakdown HEI, where the energy deposited in the breakdown phase was increased over the standard and capacitive HEI systems.

4.2 Ignition System Characteristics

The three different ignition systems used produced sparks of approximately equal energy, i.e. 60 mJ. However, by modifying the standard HEI system, different power levels, durations and energy transfer efficiencies were obtained.

As mentioned earlier, the spark plug used was a non-resistive standard plug, with an electrode diameter of 2 mm, and J-gap ground strap. The plug was mounted in the wall of the test section, with the ground strap perpendicular to the mean flow.

4.2.1 Standard HEI

The electrical characteristics of an individual discharge from the standard HEI system are shown in Figures 14-15, where the voltage, current, power, and energy time histories are shown. Due to the voltage and current values ($\tilde{}$1000 v, < .1 A), and the long duration of the spark (2.51 msec), this system was classified as predominately glow discharge.

Fifty independent measurements of the glow energy

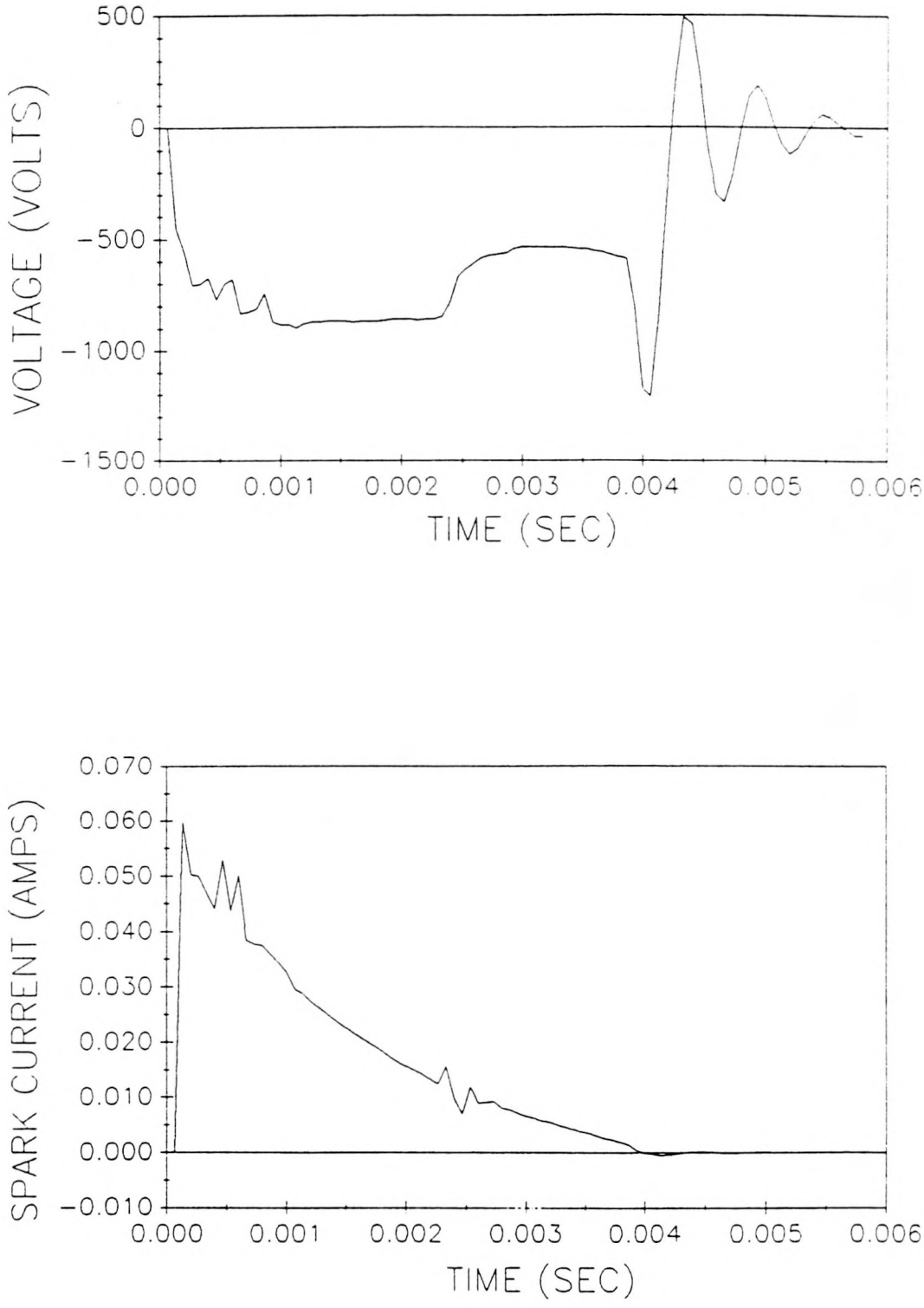

FIGURE 14: Typical voltage and current time histories of the standard HEI ignition system.

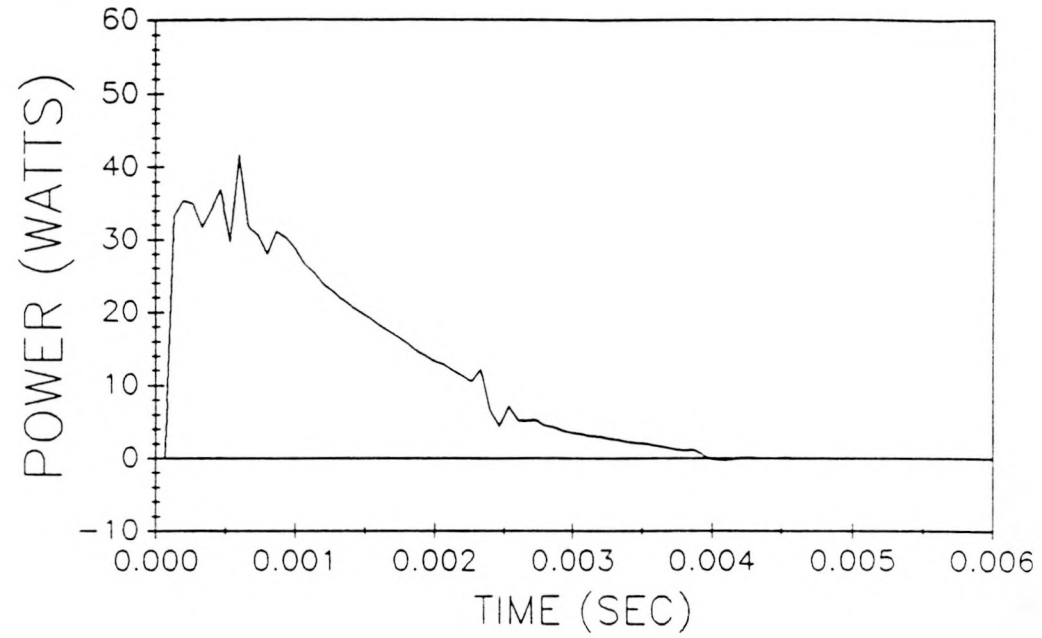

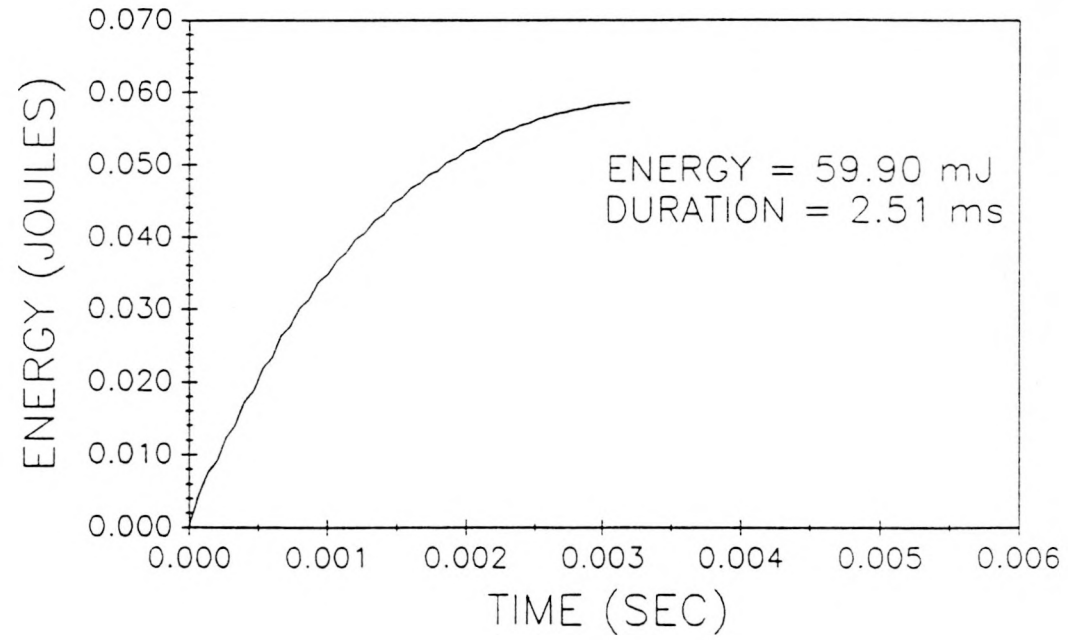

FIGURE 15: Typical power and energy time histories of the standard HEI ignition system.

were taken, with an average of 59.90 mJ, and a standard deviation of 2.77 mJ. The duration of this discharge was defined as the time when 95% of the total energy was deposited into the plasma. Using the same 50 measurements, a duration of 2.51 msec with a standard deviation of .21 msec was calculated.

As with all sparks, a breakdown phase must precede other discharges. The breakdown energy of this system was calculated directly from equation (2.5). Where the plug capacitance, C_s, was measured to be 20 pf, and the breakdown voltage, not seen in Figure 14, was recorded as 4.5 kV. With these values the breakdown energy was calculated as .20 mJ.

Referring back to Figure 2, the effective energy deposited in the glow phase can be calculated by considering its energy transfer efficiency. For a mean flow of 1.25 m/sec the glow efficiency is 8% [2]. Therefore, the effective energy of the glow phase is 4.79 mJ. The efficiency of the breakdown phase is independent of the flow velocity with a constant value of 94% [2]. Thus, in addition to the effective glow energy of 4.79 mJ, and additional .19 mJ is deposited in the breakdown phase, resulting in a total effective energy of 4.98 mJ for this system.

4.2.2 Capacitive HEI

The capacitive HEI system was constructed with the intention of producing an enhanced breakdown spark, by placing an additional capacitance of 6100 pf in parallel with the spark plug. However, after analyzing its electrical characteristics (Figures 16-17), the system was found to be more representative of a short duration glow discharge, with an increased capacitance on the secondary side of the coil. This distinction was based on the high voltage and low current levels found in a glow discharge.

As with the standard HEI system, 50 independent measurements of the energy and duration were taken. The average energy of this system was found to be 57.76 mJ with a standard deviation of 10.04 mJ. The duration of the system was calculated as .61 msec with a standard deviation of .36 msec.

The breakdown energy of this system was identical to that of the standard HEI, .20 mJ. This equality is expected since the same plug gap was used, yielding the same spark gap capacitance, and the same breakdown voltage. The energy transfer efficiency of the capacitive discharge system is the same as that of the standard HEI, i.e. 8%. Therefore, the effective energy of the capacitive glow discharge is 4.62 mJ, and the effective breakdown energy is still .19 mJ. Thus the

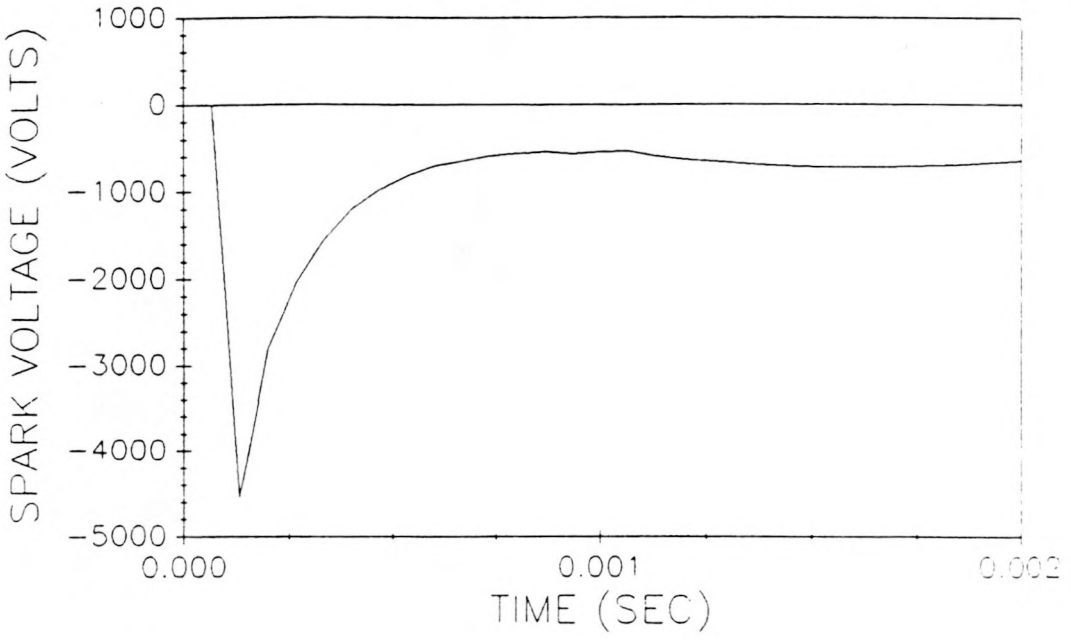

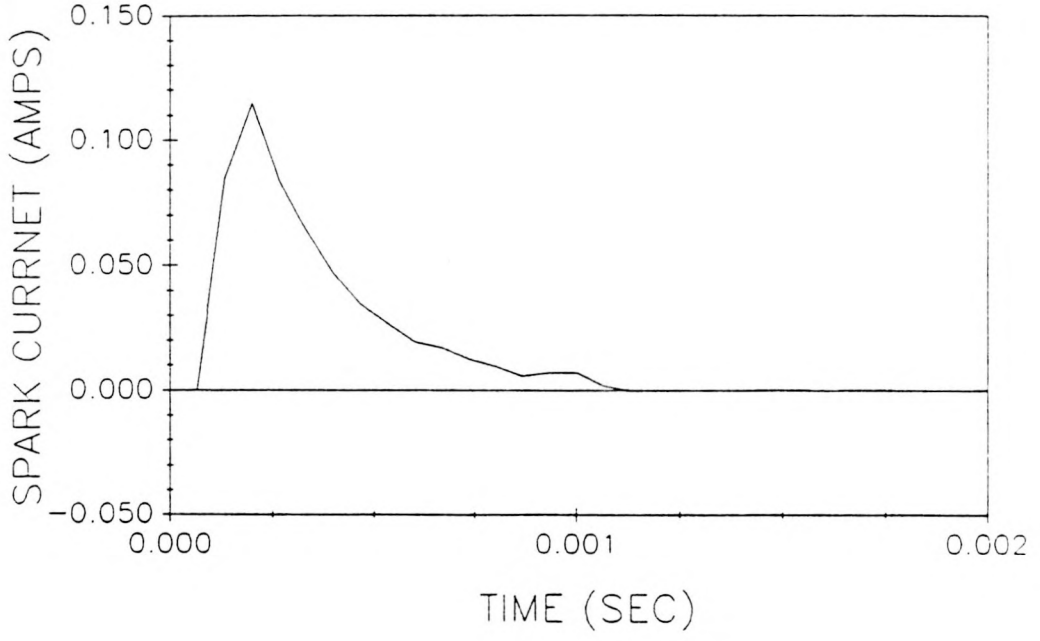

FIGURE 16: Typical voltage and current time histories of the capacitive HEI ignition system.

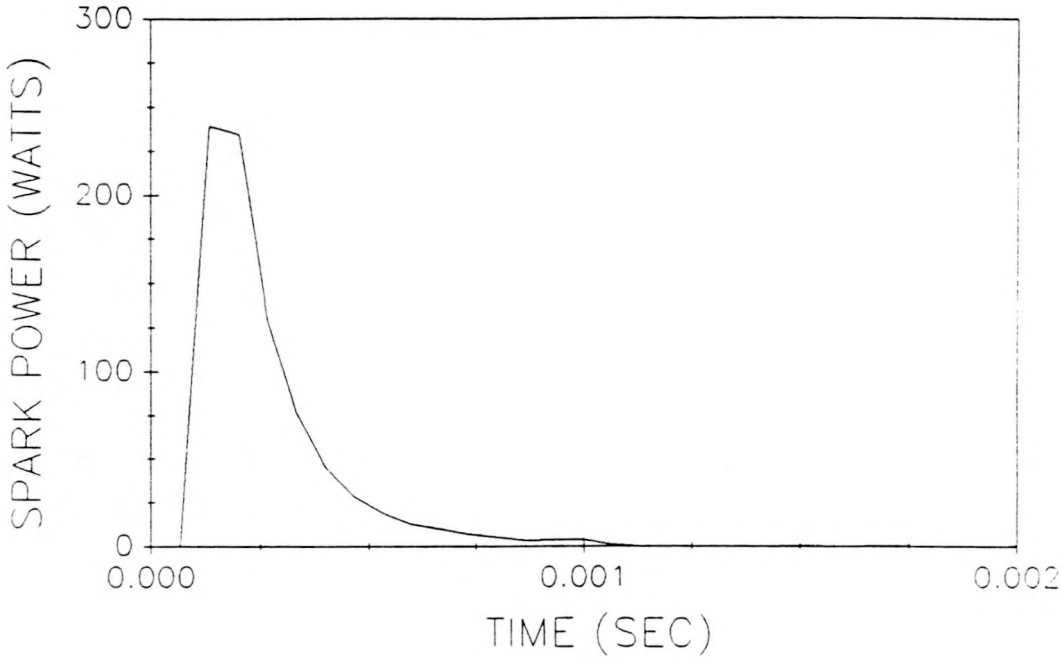

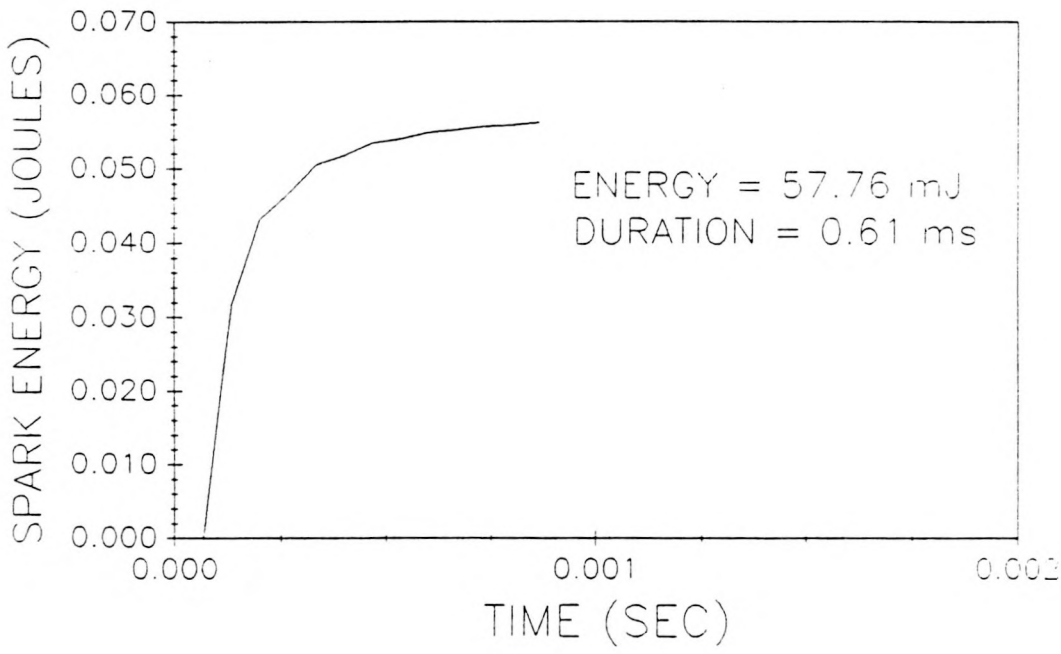

FIGURE 17: Typical power and energy time histories of the capacitive HEI ignition system.

total effective energy of this spark is 4.81 mJ.

4.2.3 Breakdown HEI

The final system used in this study was an enhanced breakdown HEI. Here, the initial breakdown energy of the system was increased by increasing the breakdown voltage to 20 kV, by using an isolation spark gap. Again, using equation (2.5), the breakdown energy of the system was calculated to be 4.0 mJ.

Due to measurement noise associated with this spark, the electrical characteristics of the spark could not be recorded with the analog to digital converter. However, if it is assumed that the energy of the HEI system is conserved, the remaining energy after the breakdown phase, approximately 56 mJ, will be deposited in the glow phase. Also, since the spark could not be recorded digitally, a value for the spark duration could not be defined. However, since more energy is deposited initially, the duration of this spark will be less than that of the standard HEI system. The net effective glow energy of this system, using the same arguments as for the other two systems, is 4.48 mJ, with an additional 3.76 mJ in the breakdown phase, yielding a total effective energy of 8.24 mJ. A summary of the ignition system characteristics is given in Table 2.

One problem encountered with the breakdown HEI system

Table II: Summary of Ignition Systems

	Standard HEI	Capacitive HEI	Breakdown HEI
Plug Capacitance	20 pf	20 pf	20 pf
Breakdown Voltage	4.5 kV	4.5 kV	20 kV
Breakdown Energy	.20 mJ	.20 mJ	4.0 mJ
Glow Energy	59.90 mJ	57.76 mJ	~56 mJ
Glow Energy Standard Deviation	2.77 mJ	10.04 mJ	
Total Energy	60.10 mJ	57.96 mJ	~60 mJ
Duration	2.51 ms	.61 ms	
Duration Standard Deviation	.21 ms	.36 ms	
Breakdown Efficiency	94%	94%	94%
Effective Breakdown Energy	.19 mJ	.19 mJ	3.76 mJ
Glow Efficiency	8%	8%	8%
Effective Glow Energy	4.79 mJ	4.62 mJ	~4.48 mJ
Total Effective Energy	4.98 mJ	4.81 mJ	~8.24 mJ

was the electromagnetic noise generated by the spark which would cause the ignition system to automatically retrigger. However, the time between retriggering (~1/2 second) was much greater than the time required for flame kernel growth (~8 msec). Therefore, the effects of the second spark had no effect on the initial spark kernel's growth.

4.3 Flame Kernel Growth Measurements

A total of 10 different ignition events were recorded and analyzed for each operating condition. For each of the three different ignition systems, two dilution cases, 0% and 15%, and two turbulence intensities, u'=.30 m/s and u'=.96 m/s were used, except for the capacitive HEI system, where only the low turbulence case was used. The plots of these 10 cases showing the individual equivalent kernel radii are given in Appendix B, while the average kernel radii, and kernel growth rate versus time are shown in Figures 18 to 27. For the individual kernel radii curves, 10 events were taken; however, for certain cases, due to experimental error with the video system, not all of the individual curves could be processed. Therefore, for some cases less than 10 events were averaged, with the lowest total being six.

The growth rate curves were calculated as the change

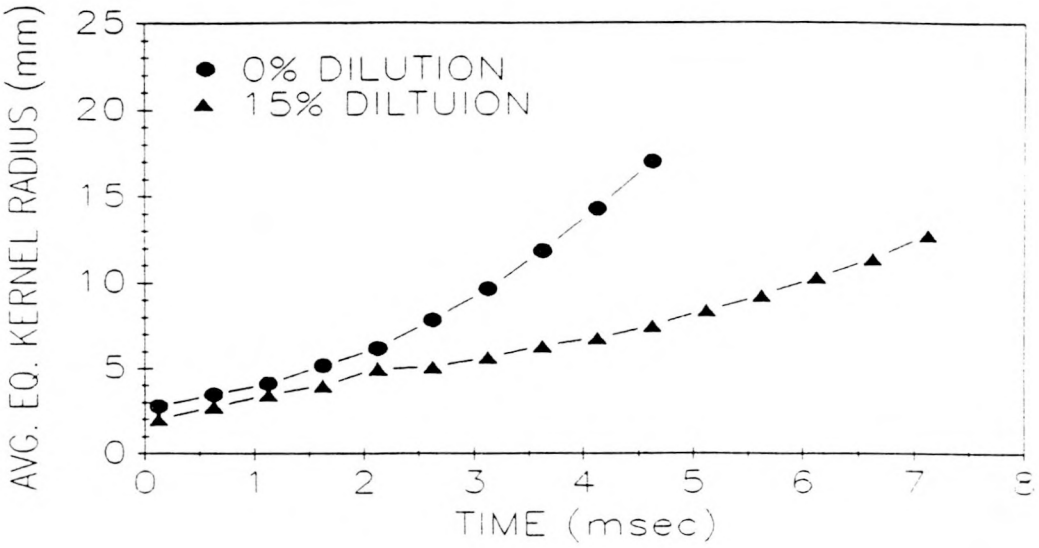

FIGURE 18: Average equivalent kernel radius vs. time for the standard HEI, effective energy 4.98 mJ, u'=.30 m/sec.

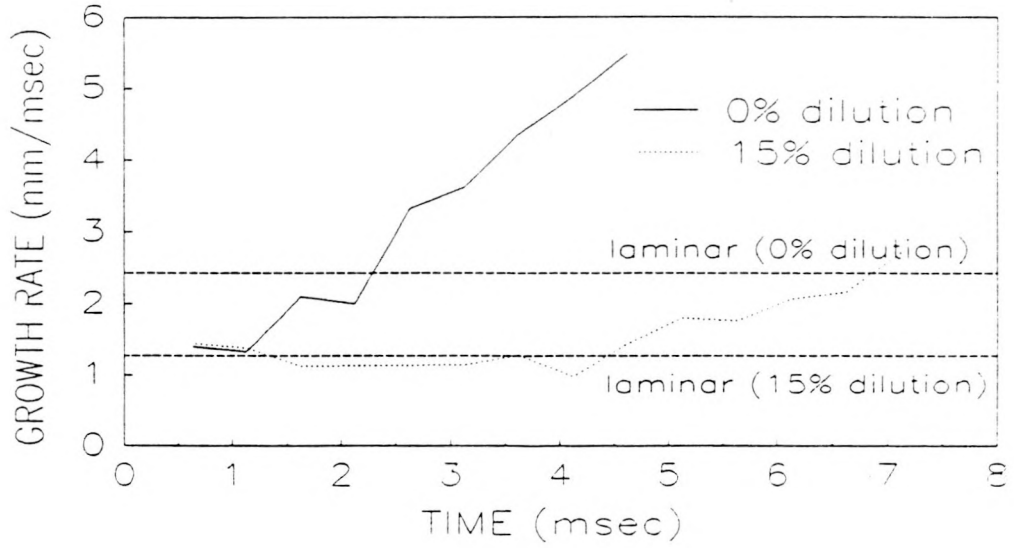

FIGURE 19: Kernel growth rate vs. time for the standard HEI, effective energy 4.98 mJ, u'=.30 m/sec.

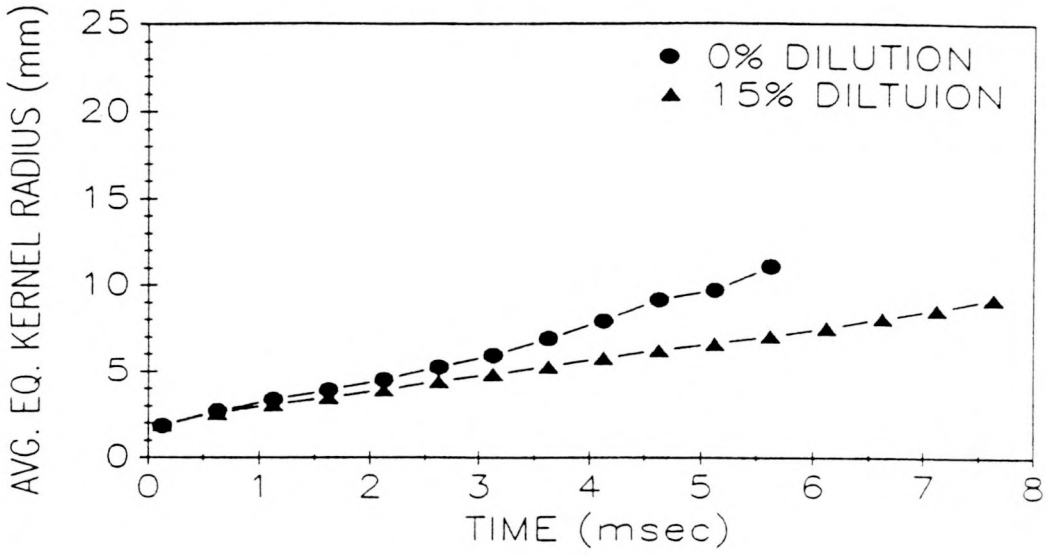

FIGURE 20: Average equivalent kernel radii vs. time for the standard HEI effective energy 4.98 mJ, u'=.96 m/sec.

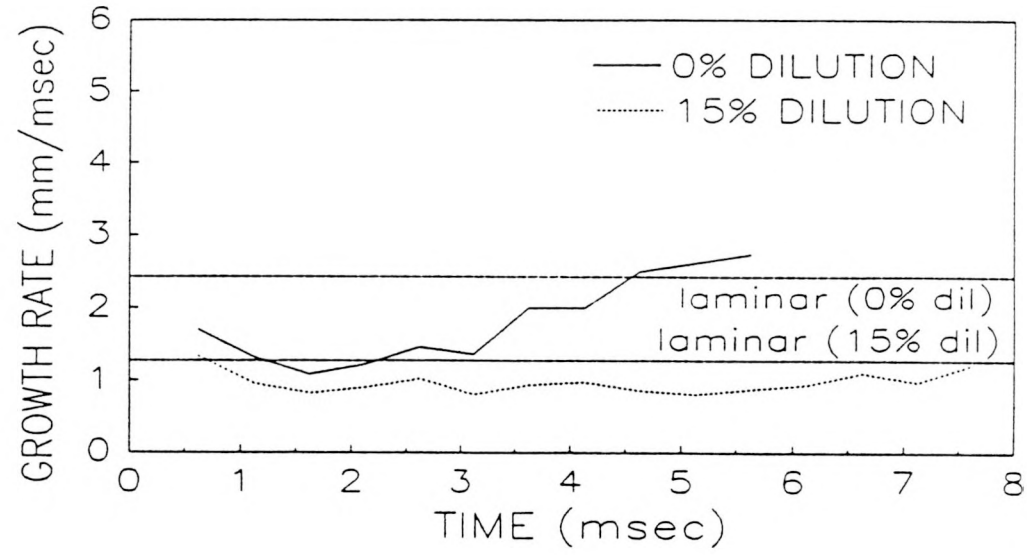

FIGURE 21: Kernel growth rate vs. time for the standard HEI, effective energy 4.98 mJ, u'=.96 m/sec.

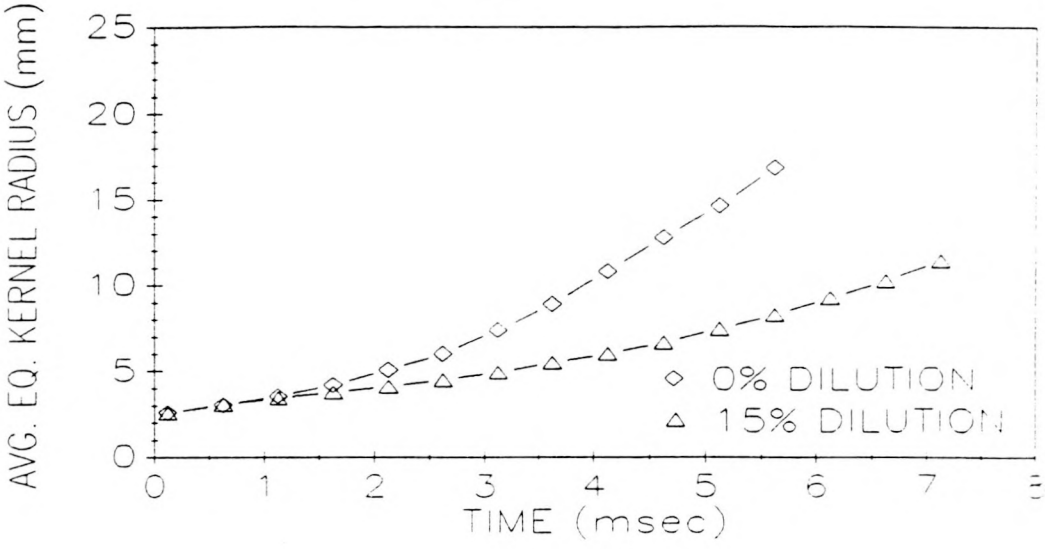

FIGURE 22: Average equivalent kernel radius vs. time for the capacitive HEI, effective energy 4.81 mJ, u'=.30 m/sec.

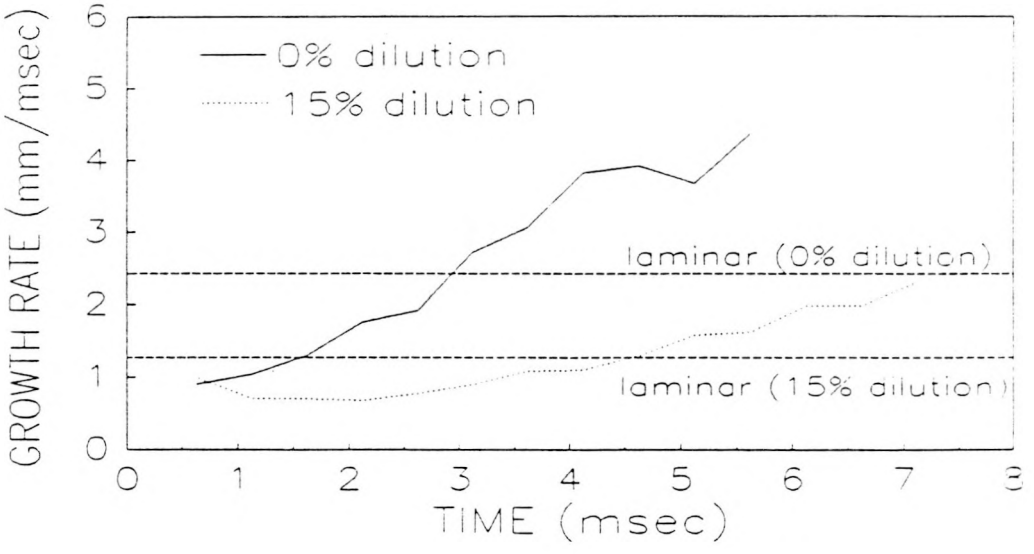

FIGURE 23: Kernel growth rate vs. time for the capacitive HEI, effective energy 4.81 mJ, u'=.30 m/sec.

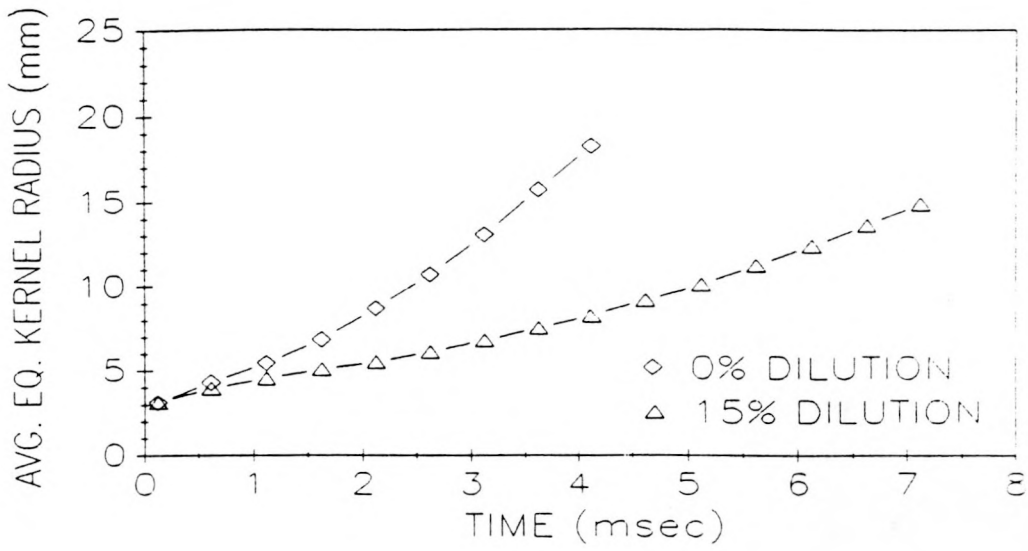

FIGURE 24: Average equivalent kernel radius vs. time, for the breakdown HEI effective energy 8.24 mJ, u'=.30 m/sec.

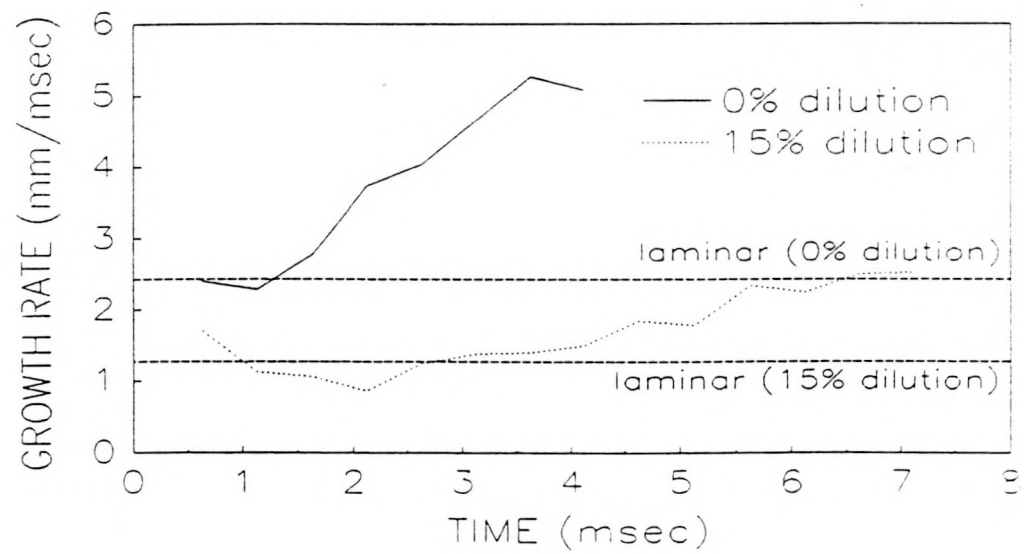

FIGURE 25: Kernel growth rate vs. time, for the breakdown HEI effective energy 8.24 mJ, u'=.30 m/sec.

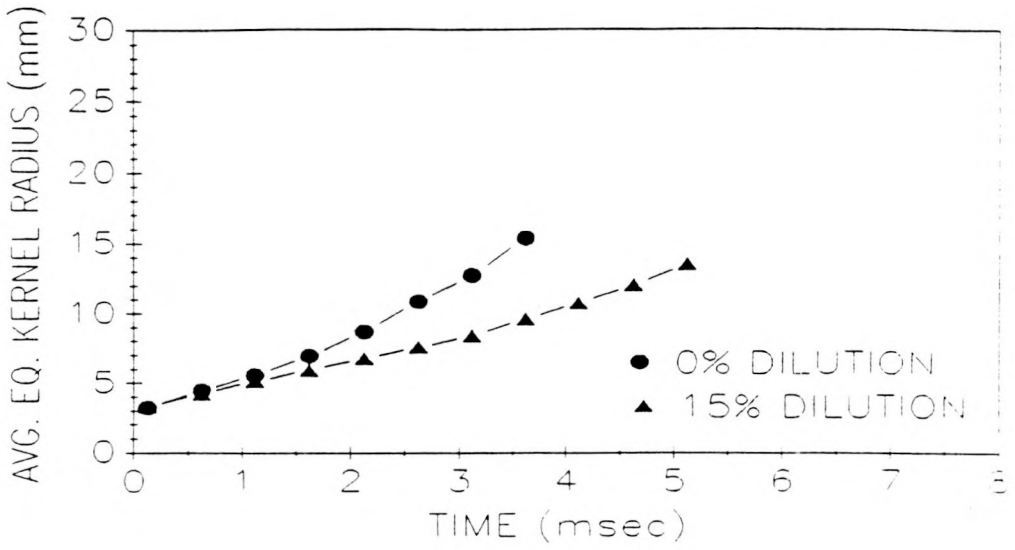

FIGURE 26: Average equivalent kernel radius vs. time, for the breakdown HEI effective energy 8.24 mJ, u'=.96 m/sec.

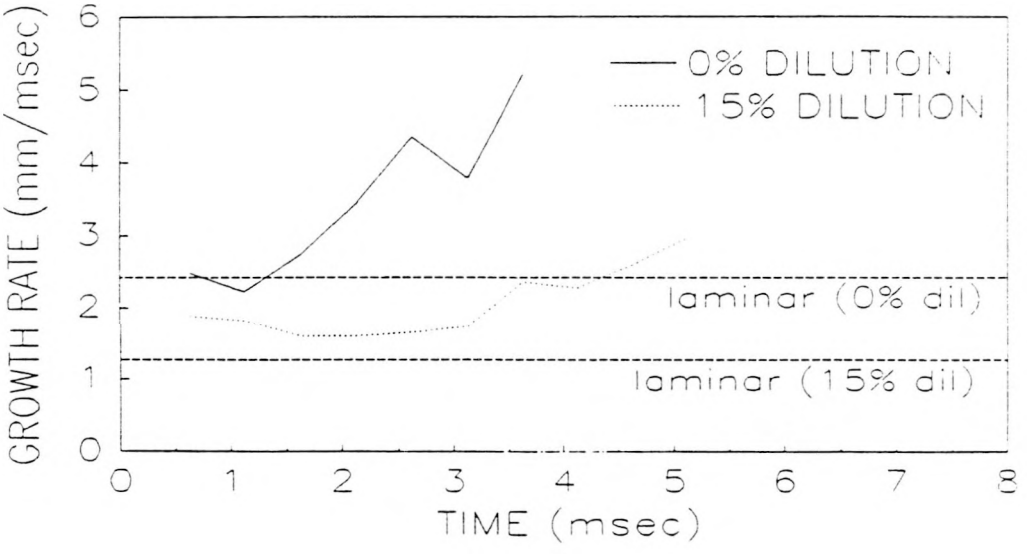

FIGURE 27: Kernel growth rate vs. time, for the breakdown HEI effective energy 8.24 mJ, u'=.96 m/sec.

in radius divided by the change in time for each successive time interval. The horizontal dashed lines shown on these figures correspond to the laminar expansion velocity.

$$dr/dt = (T_b/T_u)S_l \qquad (2.9)$$

The unburnt gas temperature was 300 K, and the burnt gas temperature, i.e. the adiabatic flame temperature, was calculated using the NASA equilibrium code [21, p. 99]. The laminar flame speeds used were obtained from reference 32. For the 15% dilution case, the flame speed was calculated using the following equation [32]

$$S_l = (1.0 - 3.0\ f)S_{lo} \qquad (4.1)$$

where f is the mixture fraction, and S_{lo} the reference flame speed for the given temperature with no dilution. This linear approximation has been shown to be applicable for the dilutions studied in this experiment [32]. The calculated laminar expansion velocities were 2.43 mm/msec for 0% dilution and 1.27 mm/msec for 15% dilution.

4.4 The Effect of the Ignition System

The ignition system affects the growth of the flame kernel in three ways. One is the effect of the breakdown process on the initial size of the flame kernel. The second is the enhancement of the mass burning rate due to the thermo-chemical state of the

flame kernel following the breakdown process. The third is the spark assisted growth due to the arc and/or glow discharge.

The initial size of the flame kernel depends primarily on the amount of breakdown energy supplied by the ignition system. If equal amounts of breakdown energy are supplied by separate sparks the initial size of the resulting flame kernels should be identical. For the standard HEI ignition system (Figures 18 and 20), and the capacitive HEI ignition system (Figure 22), the breakdown energy was .20 mJ. While for the breakdown HEI system (Figures 24 and 26), the breakdown energy was 4 mJ. Each ignition systems has a fixed breakdown energy which does not vary with dilution, and in four of the five cases no discernable difference is seen in the initial size of the kernel. Thus, when equal amounts of breakdown energy are supplied to mixtures of varying chemical composition the initial size of the flame kernels will still be identical.

When comparing different breakdown energies, increasing the breakdown energy should lead to an increase in the initial size of the flame kernel. For the standard and capacitive HEI systems (Figures 18, 20, and 22), the initial size of the kernel is between 2.0 and 2.5 mm. However, for the breakdown HEI system the initial size was 3 mm (Figures 24 and 26). Therefore,

an increase in the breakdown energy does show a noticeable increase in the initial size of the flame kernel. This increase in size is not linearly related to the increase in breakdown energy since an increase of 20 times the breakdown energy was necessary to increase the kernel size approximately 33%.

A possible reason for the discrepancy in the initial sizes of the standard and capacitive HEI systems lies in the subjectivity involved in defining the kernel boundary. The initial radii of these flame kernels are between 2.0 and 2.5 mm, which is nearly identical to the size of the electrode. Therefore, at this time approximately half of the kernel is masked by the electrode, increasing the subjectivity involved in defining the initial size.

The second process that the ignition system affects is the enhancement of the mass burning rate due to gas breakdown. For the standard and capacitive HEI systems, the initial growth rate for both dilution cases is close to 1 mm/msec (Figures 19, 21, and 23). However, when the breakdown energy is increased the initial growth rate increases and is closer to 2 mm/msec (Figures 25 and 27).

This increase in the initial growth rate takes place for two reasons. First, larger breakdown energies result in the generation of higher temperatures and

greater concentrations of chemically reactive radical and ionized species within the kernel. The resultant increased diffusion of both thermal and chemical energy into the flame front leads to a higher reaction rate and enhanced growth. In addition to the diffusion processes, the initial growth is also enhanced by a suction phase which follows the shock front [3]. When the breakdown energy of the spark is increased, the strength of the resulting shock wave also increases. The increased shock strength increases the momentum of the gas molecules behind the shock enhancing the suction phase. Then, due to friction along the electrode surfaces, larger amounts of unburned fuel and air are entrained into the kernel by the increased suction. This influx of fresh gas accelerates the burning rate since more species are available to react.

The final affect of the ignition system is on the spark assisted growth of the kernel. To characterize the effects of spark assisted growth the figures related to the low turbulence, standard and capacitive HEI ignition systems will be discussed. The breakdown HEI ignition system is neglected since its spark characteristics were not experimentally resolved. Also, the effects of turbulence are eliminated by considering only one turbulence intensity.

The main point which is evident when analyzing the

growth of the standard and capacitive HEI systems is the similarity in the early growth rates of both dilution cases when the spark is active (Figures 19 and 23). The initial growth rates of the standard HEI 0% and 15% dilution cases are actually identical for the first millisecond, indicating a spark assisted growth regime (Figure 19). The capacitive HEI case (Figure 23), also shows similarity in the growth of both dilution cases even though the curves start to diverge. For this system the duration of the spark is only .61 msec. Therefore, spark assisted growth is prevalent since the growth rates are similar up to this time. It should also be noted that during spark assisted growth the kernel size is small. When the kernel size is small, the effects of geometric stretch on the kernel's chemical heat release will be large, since stretch is inversely proportional to kernel size.

4.5 Effect of Geometric Stretch

As with spark assisted growth, geometric stretch will be discussed only for the low turbulence case to avoid the influences of turbulence. The geometric stretch rate, K, for a flame kernel was previously defined as,

$$K = (2/r)\ dr/dt \qquad (2.17)$$

where r is the kernel radius, and dr/dt is the growth rate. Therefore, when the kernel is small and the

growth rates slow, i.e. during initial growth, the effects of geometric stretch will be large.

In this experiment the standard and capacitive HEI systems (Figures 19 and 23), show the adverse effects of geometric stretch, leading to a decrease in the chemical heat release of the kernel. This fact is most noticeable for the 0% dilution cases of the two systems.

For both the standard and capacitive 0% dilution cases, the growth rates of the kernels are actually less than the laminar growth rate, indicating geometric stretch effects until approximately 3 msec. During this time, the loss of chemical energy due to the adverse effects of stretch are not offset by the electrical energy supplied by the spark, thus keeping the growth rates below the laminar value. The effects of stretch on the 0% standard HEI case last for the duration of the spark, 2.5 msec. However, for the capacitive HEI system the spark duration is very short, .61 msec, at which time the stretch rates are highest due to the small size of the kernel. Therefore, in this case all of the energy is supplied when the stretch rates are the highest and the spark energy does not overcome the stretch effects to bring the kernel growth to its laminar value. This results in stretch effects which persist until 3 msec.

The effects of geometric stretch are still present to

a lesser extent for the 15% dilution cases of the capacitive and standard HEI systems. In these cases (Figures 19 and 23), the initial growth of the kernel is near the corresponding laminar growth rate. Therefore, the amount of chemical energy lost by the kernel due to stretch is offset by the spark energy yielding a laminar growth rate for the standard HEI, and close to laminar growth for the capacitive HEI. Thus, for these two ignition systems, the loss of chemical energy due to stretch is less for the 15% dilution cases compared to the 0% dilution cases, however, the explanation for this behavior is not known.

When analyzing the initial growth rates of the low turbulence breakdown HEI system (Figure 25), both dilution cases proceed along their respective laminar growth rates. For this system, the effects of geometric stretch are not as prominent as in the standard and capacitive HEI systems, for two reasons. First, as previously discussed, the breakdown HEI system produces a larger initial flame kernel. When the kernel is larger, lower geometric stretch rates result since stretch is inversely proportional to kernel size. Secondly, the increased chemical reactivity initiated by the enhanced breakdown process overrides the heat loss from the geometric stretch effects. Therefore, the breakdown HEI system produces an initially larger, more

chemically stable flame kernel which is less susceptible to geometric flame stretch effects.

4.6 Effects of Turbulence

Following the initial period of growth, if a stable flame has formed the ignition kernel will continue to grow due to flame propagation and the related thermal expansion. During this time the effects of turbulence must be considered when characterizing trends in the growth of the flame kernel. Turbulence, due to its random nature, is the primary cause of cycle-to-cycle variations, and can either enhance the growth of the kernel by increasing its flame speed, or adversely affect kernel growth through turbulent flame stretch.

After the spark has ceased, the growth of the flame kernel will depend on its rate of chemical heat release. If the growth of the kernel is laminar, it should proceed according to equation (2.9).

$$dr/dt = (T_b/T_u)\ S_l \qquad (2.9)$$

However, if the effects of turbulence are present the turbulent flame speed S_T, replaces the laminar flame speed,

$$dr/dt = (T_b/T_u)\ S_T(t) \qquad (2.14)$$

which in the absence of turbulent flame stretch will result in an increased kernel growth rate.

When considering the growth rates for the three

ignition systems at the low turbulence intensity (Figures 19, 23 and 25), evidence of the enhancing effects of turbulence are seen as all of the growth rates proceed above their respective laminar values. The growth rates for the standard HEI case (Figure 19), cross the laminar values at 2.5 and 4.5 msec for the 0% and 15% dilution cases respectively. At these times, it is also seen that the size of the respective kernels are approximately 6 to 7 mm in radius (Figure 18). The reason for the increase in growth rate when the kernel reaches this size can be explained using a turbulent radius argument.

The argument being made is that for flame kernels whose characteristic length, i.e. radius, is less than twice the integral length scale, the kernel is convected by the turbulent flow field and growth is not enhanced. However, once the characteristic length is greater than twice the length scale, i.e. the turbulent radius, the kernel surface becomes wrinkled, gradually increasing the mass burning rate and enhancing the kernel's growth.

In this experiment the turbulent length scale was estimated to be 3 mm. Therefore, consistent with the above observation, the effects of enhanced turbulent growth should be seen when the kernel radius is approximately 6 to 7 mm. The exact same argument applies for the capacitive and breakdown HEI systems

(Figures 23 and 25). Here, when the growth rates begin to proceed above the laminar values, leading to enhance turbulent growth, the sizes of the kernels are again 6 to 7 mm in radius (Figures 22 and 24).

The effects of turbulence can either be positive leading to an enhanced growth rate, or negative, slowing the growth rate due to turbulent flame stretch effects. For the standard HEI system, if the turbulence intensity is increased from .30 m/sec to .96 m/sec, the negative effects of turbulent flame stretch are apparent. Here, both dilutions cases show that as the turbulence is increased the corresponding kernel sizes and growth rates decrease (Figures 28 to 31). In these cases, the effects of turbulent stretch are more prevalent for the 0% dilution case than the 15% case since larger differences in the kernel size and growth rates are seen for the 0% dilution case when comparing the two turbulence levels.

The turbulent flame stretch rate, K, was previously defined as

$$K = u'/\lambda_T \qquad (2.18)$$

where u' and λ_T are the turbulence intensity and Taylor microscale, respectively. Therefore, as the turbulence intensity increases the turbulent stretch rate increases. If this stretch rate is high enough, the kernel becomes severely folded, locally quenching the

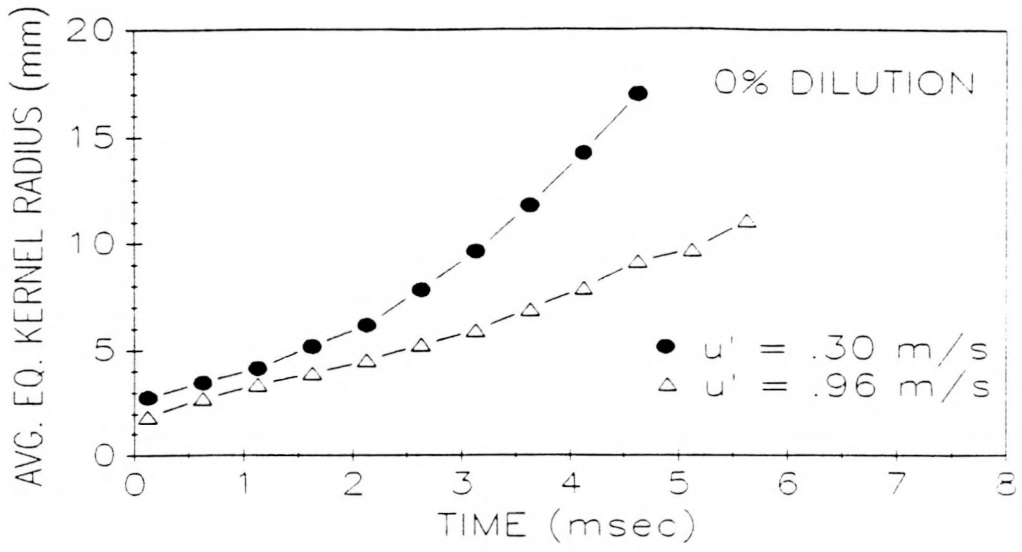

FIGURE 28: Effects of increasing turbulence intensity on kernel size for the standard HEI with 0% dilution.

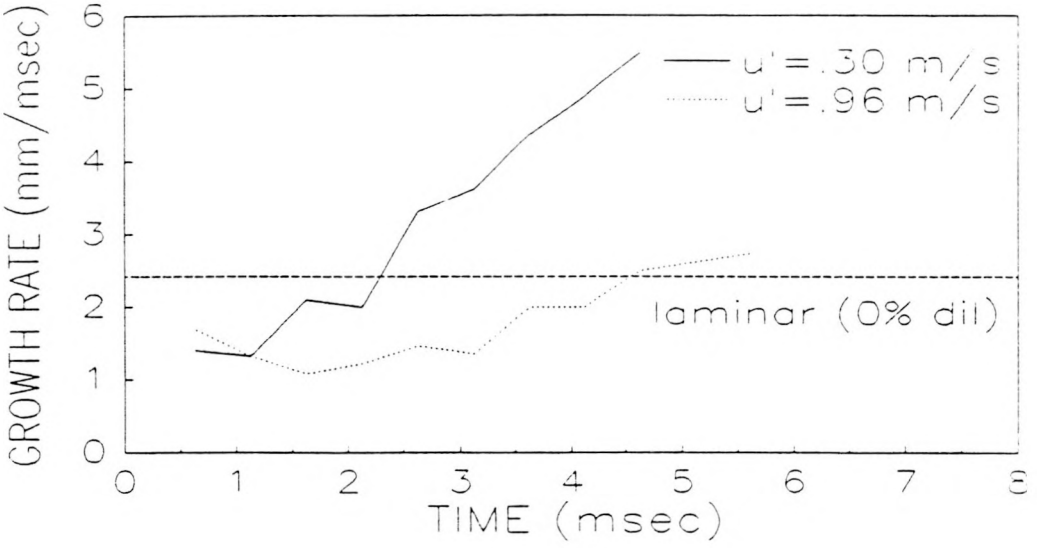

FIGURE 29: Effects of increasing turbulence intensity on kernel growth rate for the standard HEI with 0% dilution.

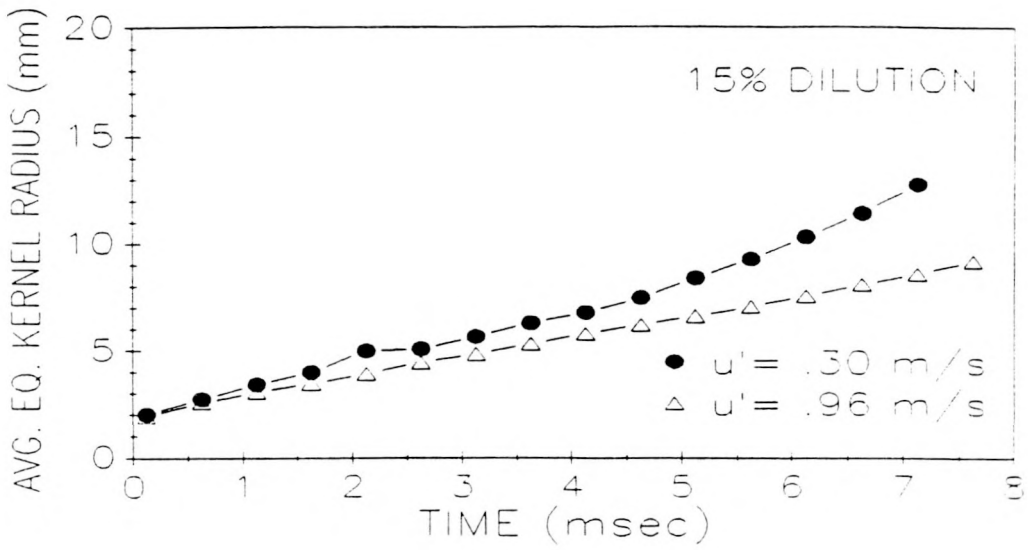

FIGURE 30: Effects of increasing turbulence intensity on kernel size for the standard HEI with 15% dilution.

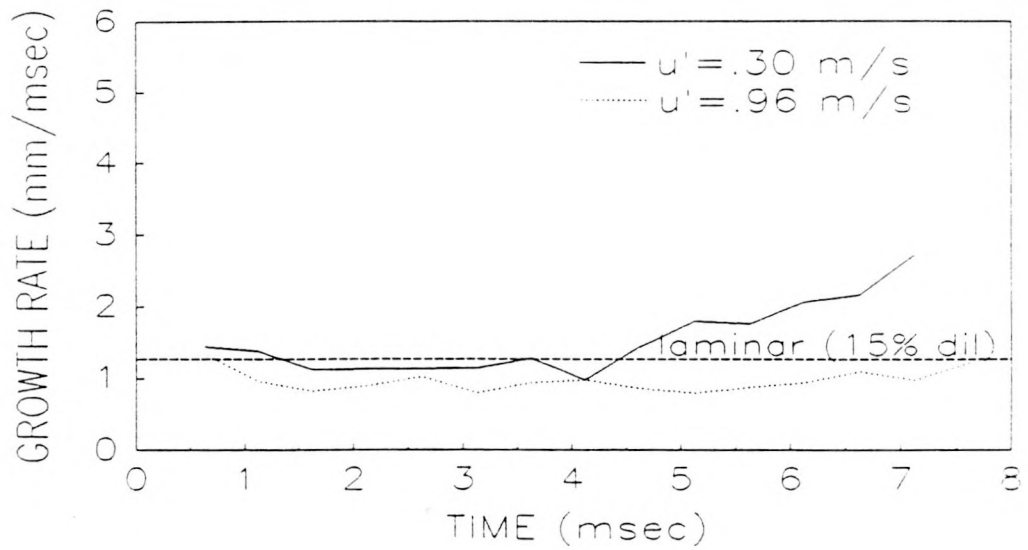

FIGURE 31: Effects of increasing turbulence intensity on kernel growth rate for the standard HEI with 15% dilution.

reaction causing a decrease of the growth rate. This explanation holds true for the standard HEI cases since an increase in the turbulence intensity resulted in slower growth rates.

The effects of increasing the turbulence intensity for the breakdown HEI system shows different trends for each of the two dilution cases (Figures 32 to 35). The 0% dilution case shows no effect on the size or growth rate of the kernel as turbulence is increased (Figures 32 and 33). However, the 15% dilution case shows the positive effects of turbulence, leading to a larger and faster growing kernel due to an increase in the mass burning rate (Figures 34 and 35). For the 0% dilution case, it can only be surmised that both the positive and negative effects of turbulence are present when the turbulence intensity is increased. If this is true, the effect of increasing the mass burning rate cancels the turbulent stretch effects netting equivalent kernel sizes and growth rates for both turbulence intensities. One observation that can be made from the two dilution cases is that the effects of increasing the turbulence intensity have a more negative effect on the 0% dilution case than the 15% dilution case. This observation is consistent with those made for the standard HEI system.

When comparing the effects of increasing turbulence on the standard HEI versus the breakdown HEI, the

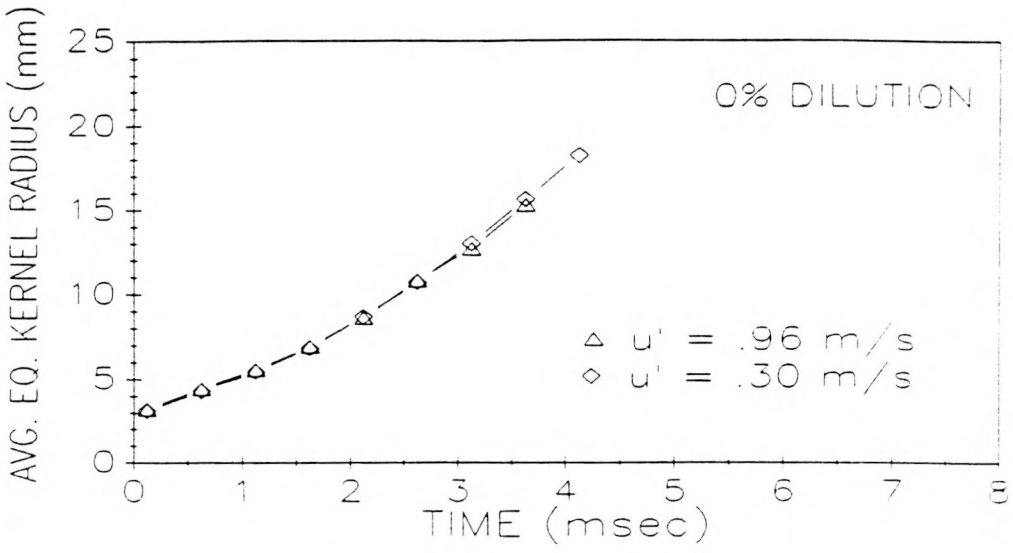

FIGURE 32: Effects of increasing turbulence intensity on kernel size for the breakdown HEI with 0% dilution.

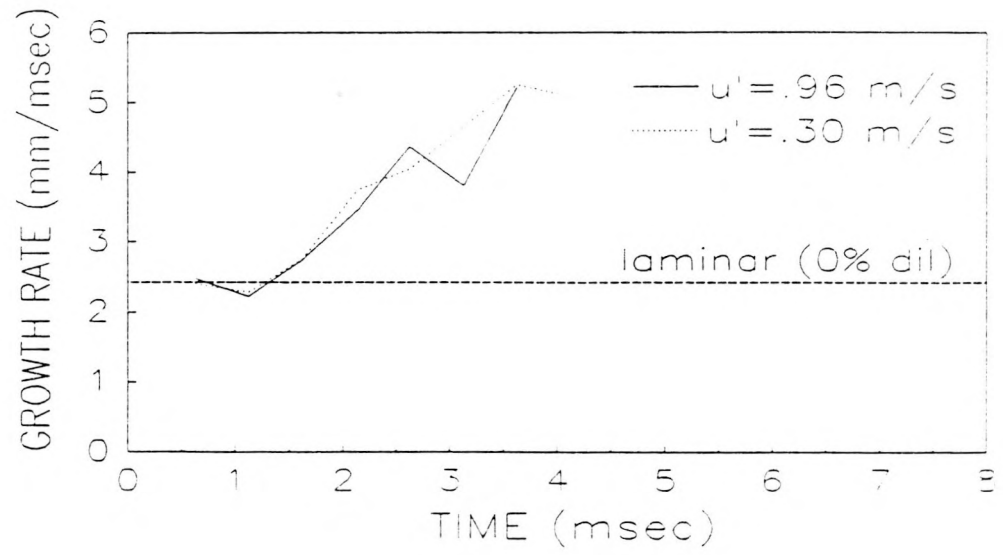

FIGURE 33: Effects of increasing turbulence intensity on kernel growth rate for the breakdown HEI with 0% dilution.

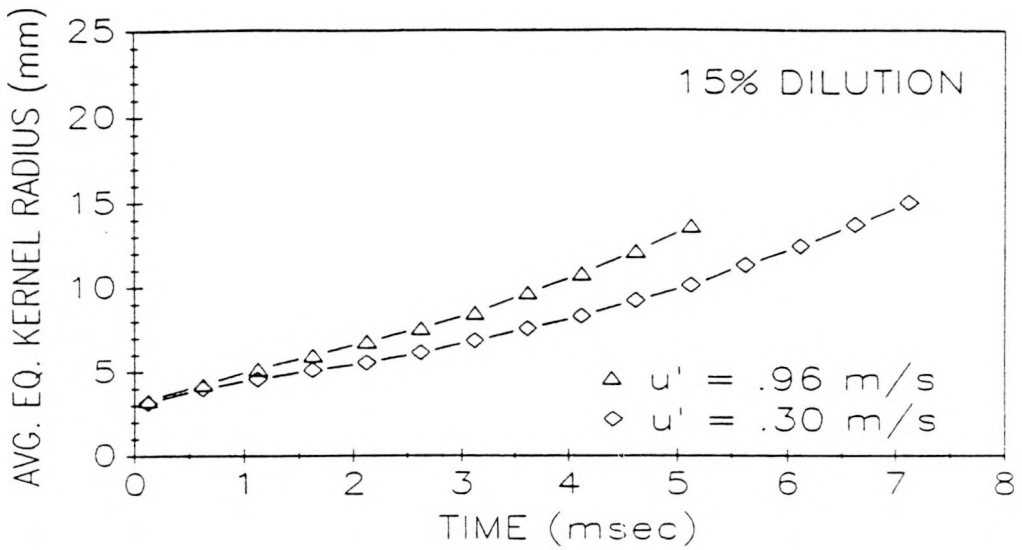

FIGURE 34: Effects of increasing turbulence intensity on kernel size for the breakdown HEI with 15% dilution.

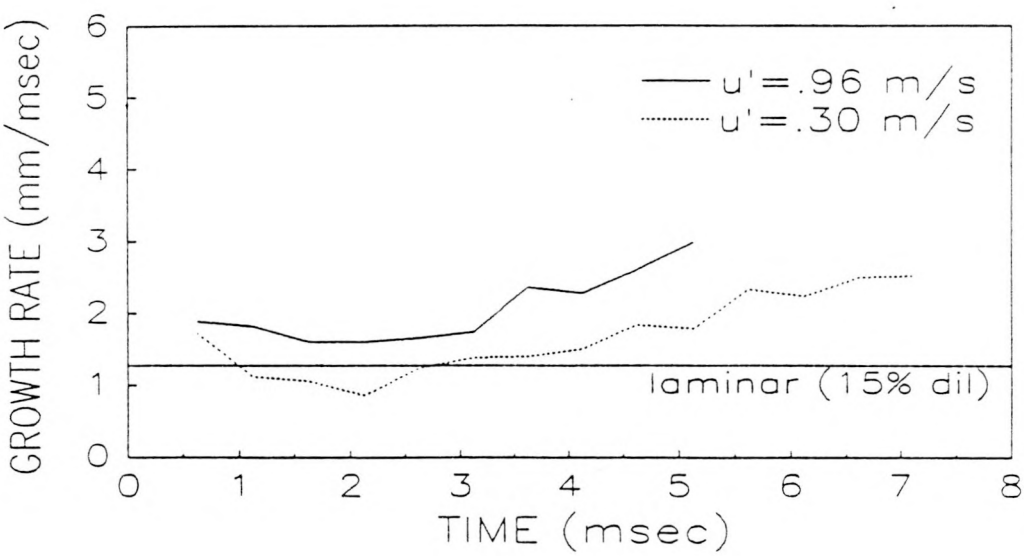

FIGURE 35: Effects of increasing turbulence intensity on kernel growth rate for the breakdown HEI with 15% dilution.

breakdown HEI system shows more resistance to turbulent stretch effects. The standard HEI system shows a degradation of growth for both dilution cases as the turbulence intensity rises. However, the breakdown HEI system showed no net effect of turbulence for the 0% dilution case, and a positive effect of turbulence for the 15% dilution case. Therefore, the higher temperatures and radical concentrations along with the enhanced suction phase of the breakdown system result in kernels which are less susceptible to turbulent flame stretch effects.

4.7 Effects of Dilution

One trend that is apparent for all of the cases considered is the effect of dilution on flame kernel growth when kernel growth depends solely on the chemical heat release of the flame (Figures 19, 21, 23, 25, and 27). For propagating flame kernels, the presence of dilution lowers the growth rate of the kernel by lowering the flame speed and flame temperature, where the lower flame temperature reduces the expansion velocity of the kernel. This slower growth rate is a result of the reduced heat release of the mixture per unit volume when dilution is present. This fact is observed for each ignition system and turbulence level, in that the growth rates of the 15% dilution cases are

always less than their 0% counterpart, after the region of spark assisted growth.

4.8 Comparison of Cycle-to-Cycle Variations

One of the objectives of this research was to analyze the effects of cycle-to-cycle variations on flame kernel growth, with the intention of determining the best ignition system for a given operating condition which would reduce such variations. To determine the optimum ignition system, the effects of turbulence and the ignition system on cycle-to-cycle variations should be analyzed.

To quantitatively describe cycle-to-cycle variations, the standard deviation of the kernel radius was calculated. This quantity is indicative of the cycle-to-cycle variations in that the lower the standard deviation of the kernel radii, the lower the cycle-to-cycle variations, yielding a more repeatable kernel growth.

The first variable which will be examined to determine its influence on cycle-to-cycle variations is turbulence. Figures 36 to 39 show the effects of increasing turbulence on cycle-to-cycle variations for both dilution cases of the standard and breakdown HEI ignition systems. The standard HEI system with 0% dilution (Figure 36), shows a pronounced effects of

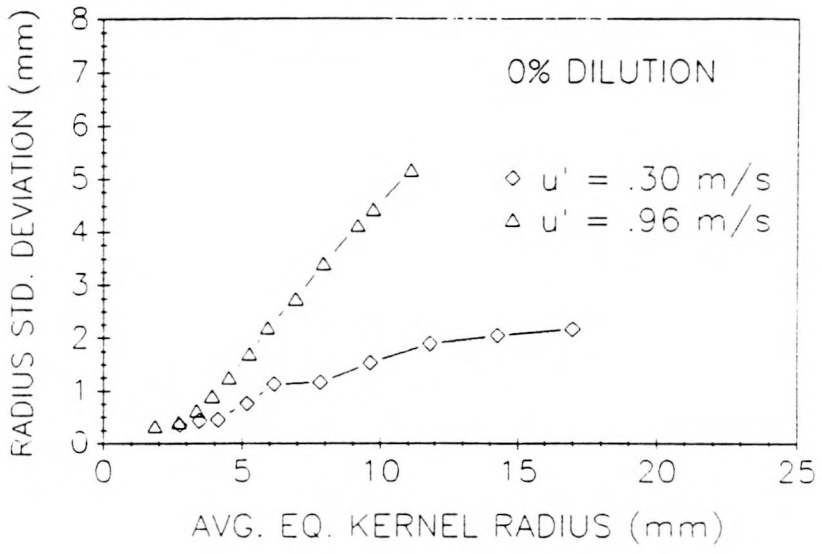

FIGURE 36: Effects of increasing turbulence intensity on kernel radii standard deviation for the standard HEI with 0% dilution.

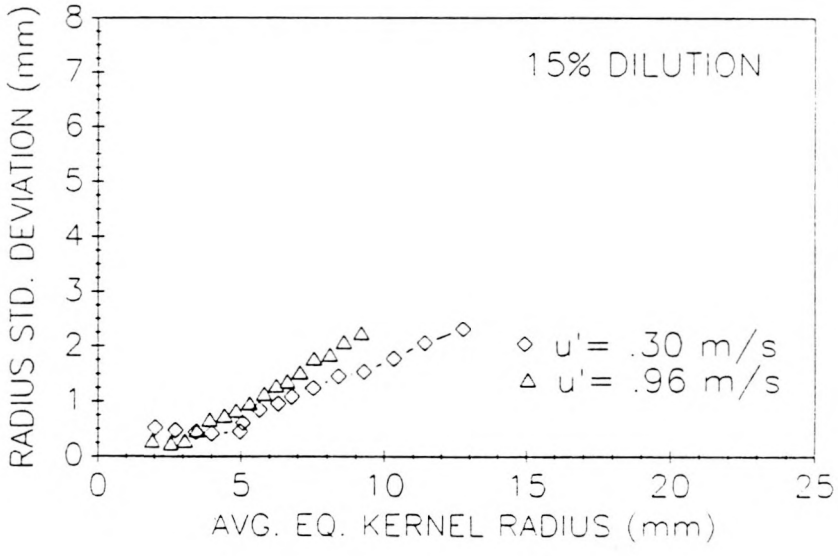

FIGURE 37: Effects of increasing turbulence intensity on kernel radii standard deviation for the standard HEI with 15% dilution.

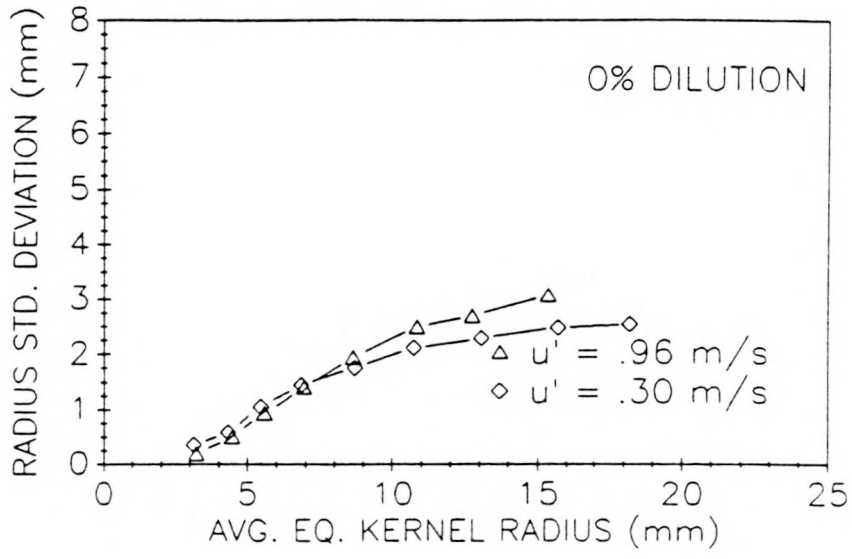

FIGURE 38: **Effects of increasing turbulence intensity on kernel radii standard deviation for the breakdown HEI with 0% dilution.**

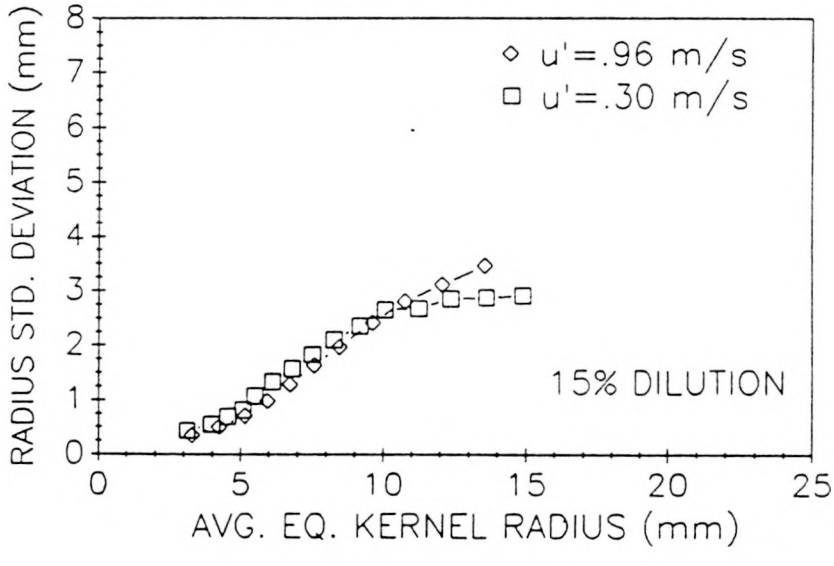

FIGURE 39: **Effects of increasing turbulence intensity on kernel radii standard deviation for the breakdown HEI with 15% dilution.**

increasing turbulence on cycle-to-cycle variations as the kernel radii standard deviations increase dramatically. This same trend to a lesser extent is also seen for Figures 37 to 39, in that when the kernel is small the effects of increasing turbulence on cycle-to-cycle variations are small. However, as the kernel grows in size the cycle-to-cycle variations of the high turbulence case always exceed the variations of the low turbulence case. This leads to the observation that cycle-to-cycle variations are lower when the turbulence intensity is lower.

Another trend which is observed from Figures 36 to 39 is that the breakdown HEI system is more resistant to cycle-to-cycle variations than the standard HEI as the turbulence intensity is increased. When the turbulence intensity is low, all dilution cases show radii standard deviations which are similar in magnitude. At the higher turbulence intensity the breakdown HEI still shows cycle-to-cycle variations which are comparable to the low turbulence case. However, the standard HEI system with 0% dilution shows a large increase in the cycle-to-cycle variations when turbulence is increased.

When comparing cycle-to-cycle variation of the three different ignition systems it is again observed that, when the turbulence intensity is low, the radii standard deviations are low, with little difference between the

ignition systems (Figures 40 and 41). As the turbulence increases a difference in the cycle-to-cycle variations of the ignition systems is noticed with the breakdown HEI having the lowest cycle-to-cycle variations (Figures 42 and 43).

As previously mentioned, the goal of this research was to determine the best ignition system which would lead to the lowest cycle-to-cycle variations for a given operating condition. From the aforementioned observations, the choice of the ignition system depends on the operating conditions.

When the turbulence intensity is low, the optimum ignition system for reducing cycle-to-cycle variations would be the standard HEI. This system has the lowest variations for the 0% dilution case (Figure 40), and is comparable to the capacitive HEI at 15% dilution (Figure 41). However, when comparing the standard HEI to the breakdown HEI, a trade-off is present. Even though the standard HEI does reduce cycle-to-cycle variations, it has a slower growth rate than the breakdown HEI (Figures 44 and 45). This more rapid growth rate would aid in the reduction of hydrocarbon emissions in engines at idle where ignition is a marginal condition. When considering the high turbulence case, the clear choice of the best ignition system is the breakdown HEI (Figures 42 and 43). The cycle-to-cycle variations for

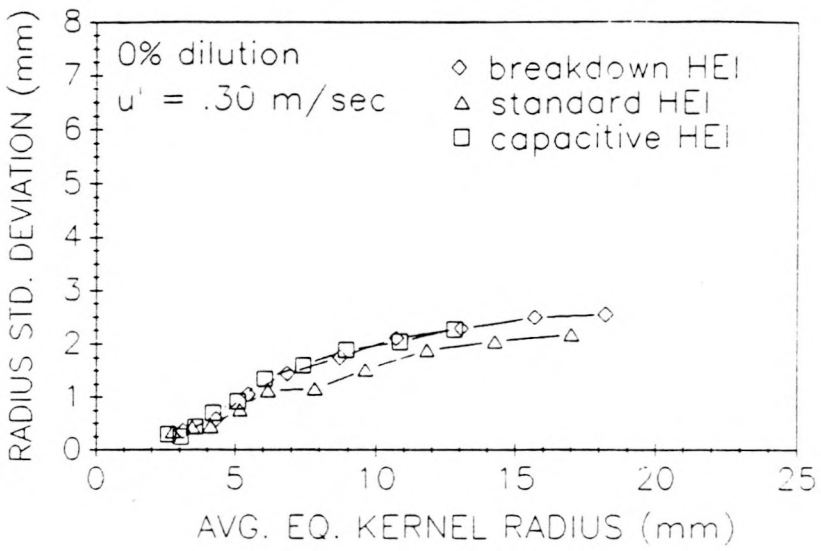

FIGURE 40: Comparison of kernel radii standard deviation for the three ignition systems with 0% dilution and u'=.30 m/sec.

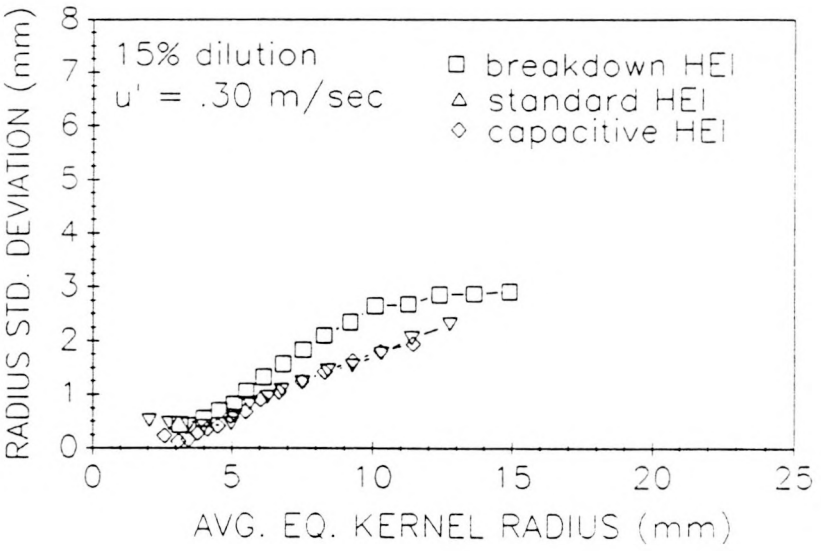

FIGURE 41: Comparison of kernel radii standard deviation for the three ignition systems with 15% dilution and u'=.30 m/sec.

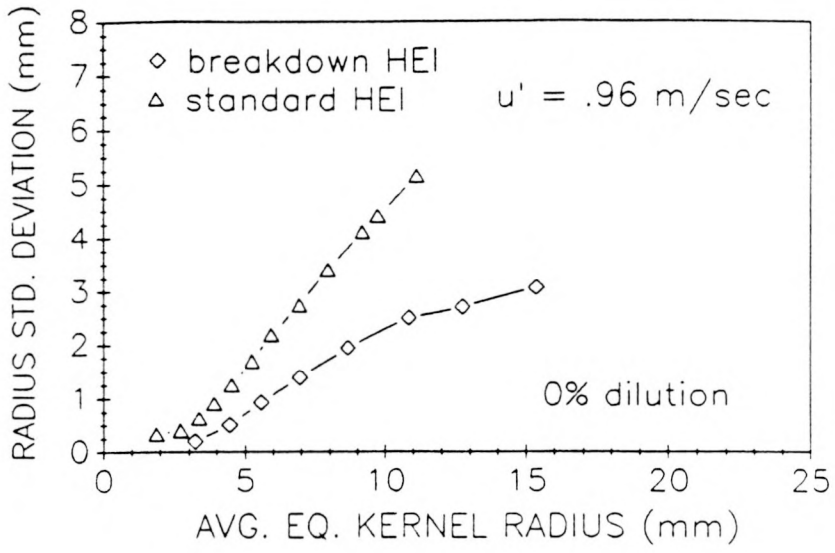

FIGURE 42: **Comparison of the kernel radii standard deviation for the standard and breakdown HEI systems with 0% dilution and u'=.96 m/sec.**

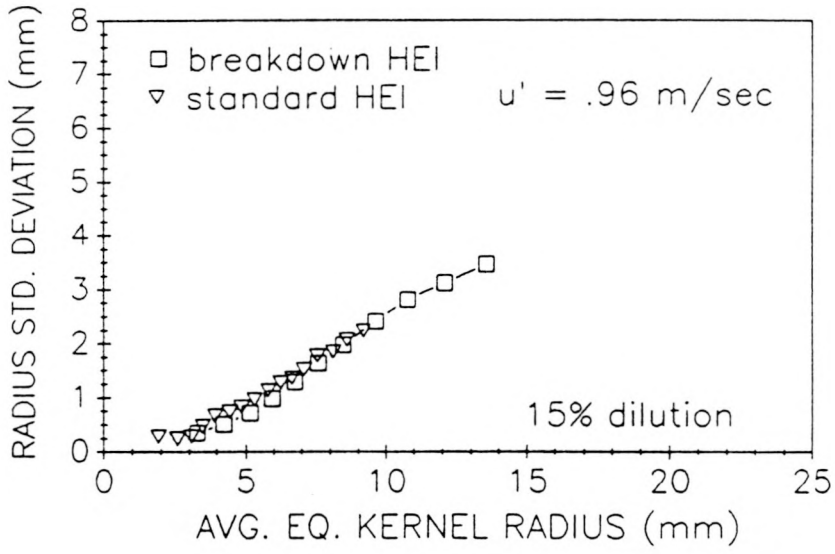

FIGURE 43: **Comparison of the kernel radii standard deviation for the standard and breakdown HEI systems with 15% dilution and u'=.96 m/sec.**

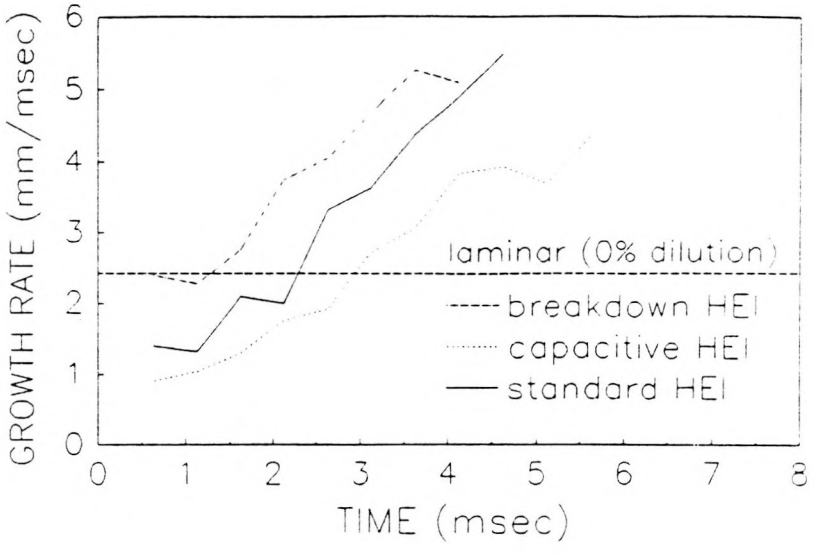

FIGURE 44: Comparison of kernel growth rates for three ignition systems with 0% dilution and u'=.30 m/sec.

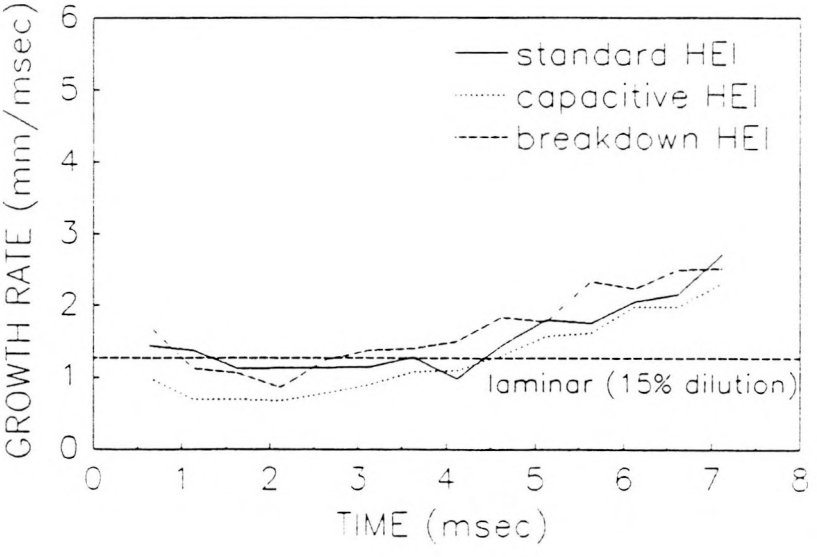

FIGURE 45: Comparison of kernel growth rates for the three ignition systems with 15% dilution and u'=.30 m/sec.

this system at both dilution levels are lower than the standards HEI's. This fact coupled with the faster growth rate of the breakdown system makes it the best choice.

If one had to choose an overall optimum ignition system for a range of operating conditions, i.e. varying turbulence intensities and dilutions, the choice would be the breakdown HEI for three reasons. First, it has the fastest growth rates of the three ignition systems (Figures 44 to 47), reducing hydrocarbon emissions. Secondly, it is the most repeatable with varying turbulence (Figures 38 and 39). The effect of changing the turbulence intensity does not significantly alter the cycle-to-cycle variations. Finally, when the turbulence intensity is low it shows comparable cycle-to cycle-variations to the other ignition systems (Figure 40 and 41), and actually shows fewer variations when the turbulence intensity is high (Figures 42 and 43).

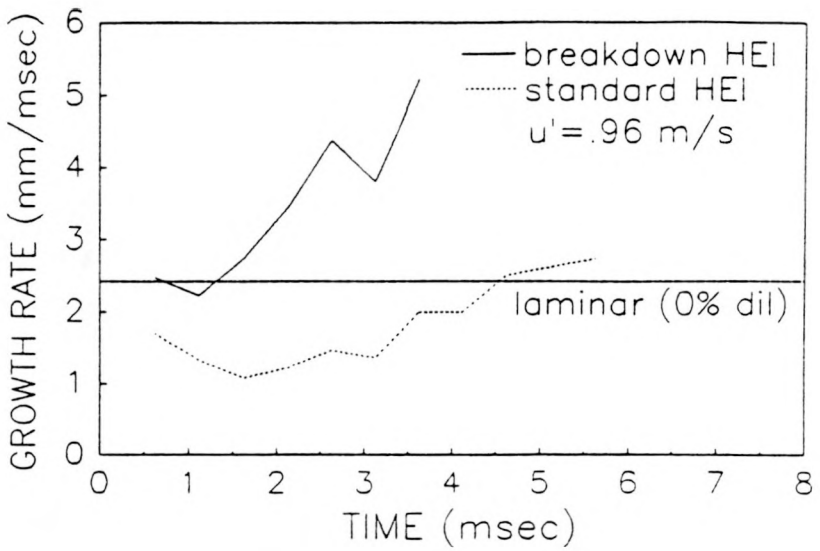

FIGURE 46: Comparison of kernel growth rates for the breakdown and standard HEI systems with 0% dilution and u'=.96 m/sec.

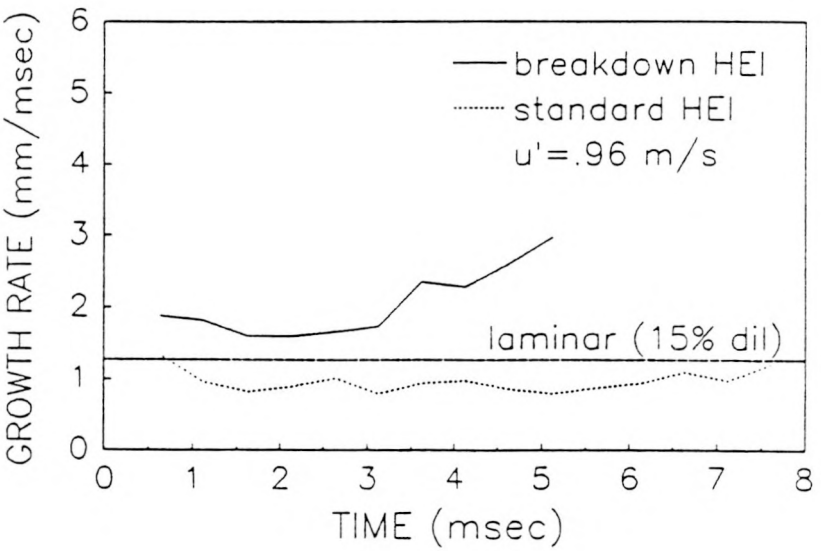

FIGURE 47: Comparison of kernel growth rates for the breakdown and standard HEI systems with 15% dilution and u'=.96 m/sec.

Chapter 5

SUMMARY

While conducting this research, the following observations were made concerning flame kernel growth under idle simulated conditions which were consistent with previous investigators' results.

1. When equal amounts of breakdown energy are supplied to mixtures of varying chemical composition the resulting initial flame kernel size will be identical.
2. Increasing the breakdown energy increases the initial flame kernel size.
3. Increasing the breakdown energy also results in higher initial growth rates due to higher temperatures and greater radical concentrations, as well as an enhanced suction phase.
4. While the spark is active a regime of spark assisted growth exists, yielding similar growth rates for mixtures with different dilutions.
5. The effects of turbulence can either be positive leading to an enhanced growth rate, or negative, slowing the growth rate due to turbulent stretch effects.
6. The effect of dilution was the same for all three ignition systems. Dilution leads to slower

growth rates resulting from the reduced heat release of the mixture.

7. When the turbulence intensity is low, the resulting cycle-to-cycle variations are low.
8. Cycle-to-cycle variations increase as the turbulence intensity increases.
9. The breakdown HEI system produced the fastest growing flame kernels.

In addition, the following observations were not previously discussed by other investigators.

10. When the kernel is small and the growth rates slow, the effects of geometric stretch are high. The effects of geometric stretch were most noticeable for the 0% dilution cases of the standard and capacitive HEI systems, resulting in slower than laminar growth rates. For the 15% dilution cases the effects of geometric stretch were offset by the spark energy input.
11. The effects of geometric stretch were not noticed for the breakdown HEI system. This system produced a more stable flame kernel which was less susceptible to geometric stretch effects.
12. For all three ignition systems, the effect of turbulent flame stretch was more prevalent for 0% dilution than 15% dilution.

13. The breakdown HEI system showed more resistance to turbulent flame stretch effects. Its kernels were more stable and less susceptible to turbulent stretch effects.
14. When turbulence intensity is low, the standard HEI system produces the smallest amount of cycle to cycle variations.
15. When the turbulence intensity is high, the breakdown HEI system produces the smallest amount of cycle-to-cycle variations.
16. Overall, the breakdown HEI systems is the best ignition system for reducing cycle-to-cycle variations over a broad range of operating conditions.

For future work, additional operating conditions should be studied. To better understand the role of the ignition system, an arc discharge spark should be studied. Also, a laminar, and an intermediate turbulence intensity flow condition should be analyzed to better understand the varying effects of turbulence on flame kernel growth. Also, to actually understand idle ignition, the experiments should be conducted in an engine. Here, the effects of the flow condition should be analyzed by varying it in ways which are common to the automotive industry, i.e., by using high and low swirl and squish conditions.

REFERENCES

[1] Cobine, J.D., Gaseous Conductors, McGraw-Hill, New York, 1941.

[2] Maly, R.R., "Spark Ignition, Its Physics and Effect on the Internal Combustion Process," in: Fuel Economy: Road Vehicles Powered by Spark-Ignition Engines, Eds., Hillard, J.C., and Springer, G.S., Chapter III, Plenum Press, 1984.

[3] Maly, R., and Vogel, M., "Initiation and Propagation of Flame Fronts in Lean CH_4-Air Mixtures by the Three Modes of the Ignition Spark," Proceedings of the Seventeenth Symposium (International) on Combustion, pp. 821-831, The Combustion Institute, 1979.

[4] Ziegler, G.F.W., Wagner, E.P., and Maly, R.R., "Ignition of Lean Methane-Air Mixtures by High Pressure Glow and Arc Discharges," Proceeding of the Twentieth Symposium (International) on Combustion, pp. 1817-1824, The Combustion Institute, 1984.

[5] Compton, K.T., AIEE Transactions, Vol. 46, p. 868, 1927.

[6] Teets, R.E., and Sell, J.A., "Calorimetry of Ignition Sparks," SAE paper 880204, 1988.

[7] Strid, K.G., "Experimental Techniques for the Determination of Ignition Energy," Oxidation and Combustion Reviews, Vol. 6, pp. 1-46, 1973.

[8] Pischinger, S., and Heywood, J., "A Study of Flame Development and Engine Performance with Breakdown Ignition Systems in a Visualization Engine," SAE paper 880518, 1988.

[9] Anderson, R.W., "Effects of Ignition System Power on Fast Burn Engine Combustion," SAE paper 870549, 1987.

[10] Ho, C.M., and Santavicca, D.A., "Turbulence Effects on Early Flame Kernel Growth," SAE paper 872100, 1987.

[11] Santavicca, D.A., "Turbulence Effects on Ignition Flame Kernel Growth," Invited paper, 1988 Fall Technical Meeting, Eastern States Section of the Combustion Institute, December, 1988.

[12] Bradley, D., and Lung, F.K-K., "Spark Ignition and the Early Stages of Turbulent Flame Propagation," Combustion and Flame, Vol. 69, pp. 71-93, 1987.

[13] Lintin, D.R., and Woodling, E.R., "Investigation of the Ignition of a Gas by an Electric Spark," British Journal of Applied Physics, Vol. 10, pp. 159-166, 1959.

[14] Chomiak, Jerzy, "Flame Development from an Ignition Kernel in Laminar and Turbulent Homogeneous Mixtures," Proceedings of the Seventeenth Symposium (International) on Combustion, pp. 255-263, The Combustion Institute, 1979.

[15] Bradley, D., Hynes, J., Lawes, M., and Sheppard, C.G.W., "Limitations to Turbulence-Enhanced Burning Rates in Lean Burn Engines," Proceedings of the Institution of Mechanical Engineers, International Conference, Combustion in Engines - Technology and Applications, 1988.

[16] Olsen, H.L., Edmonson, R.B., and Gayhart, E.L., "Microchronometric Schlieren Study of Gaseous Expansion from an Electric Spark," Journal of Applied Physics, Vol. 23, No. 10, pp. 1157-1162, 1952.

[17] Tagalian, J., and Heywood, J., "Flame Initiation in a Spark-Ignition Engine." Combustion and Flame, Vol. 64, pp. 243-246, 1986.

[18] de Soete, G.G., "Initial Burning Velocity of Spark Ignited Flames Measured by a Laser Tomography Technique," presented at the Central States Section, The Combustion Institute, March, 1981.

[19] Lim, M.T., "Spark Kernel Development in Constant Volume Combustion," PhD Thesis, The University of Michigan, Ann Arbor, 1985.

[20] Champion, M., Deshaies, B., Joulin, G., and Kinoshita, K., "Spherical Flame Initiation: Theory Versus Experiments for Lean Propane-Air Mixtures," Combustion and Flame, Vol. 65, pp. 319-337, 1986.

[21] Kuo, K.K., Principles of Combustion, John Wiley and Sons Inc., 1986.

[22] Metghalchi, M., and Keck, J., "Laminar Burning Velocity of Propane-Air Mixtures at High Temperature and Pressure," Combustion and Flame, Vol. 38, pp. 143-154, 1980.

[23] Ryan, T.W. III., and Lestz, S.S., "The Laminar Burning Velocity of Isooctane, N-Heptane, Methanol, Methane, and Propane at Elevated Temperature and Pressures in the Presence of a Diluent," SAE paper 800103, 1980.

[24] Morgan, G.H., and Kane, W.R., "Some Effects of Inert Diluents on Flame Speed and Temperatures," Proceedings of the Fourth Symposium (International) on Combustion, pp. 313-320, Williams and Wilkins Co., 1953.

[25] Egerton, A., and Sen, D., "Flame Propagation: The Influence of Pressure on the Burning Velocities of Flat Flames," Proceedings of the Fourth Symposium (International) on Combustion, pp. 321-328, Williams and Wilkins Co., 1953.

[26] Gibbs, G.J., and Calcote, H.F., "Effects of Molecular Structure on Burning Velocity," Journal of Chemical and Engineering Data, Vol. 5, pp. 226-237, 1959.

[27] Reynolds, T., and Gerstein, M., "Influence of Molecular Structure of Hydrocarbons on Rate of Flame Propagation," Proceedings of the Third Symposium (International) on Combustion, pp. 190-194, Williams and Wilkins Co., 1949.

[28] Pope S.B., and Cheng, W.K., "Statistical Calculations of Spherical Turbulent Flames," Proceedings of the Twenty-First Symposium (International) on Combustion, pp. 1473-1481, The Combustion Institute, 1986.

[29] Law, C.K., "Dynamics of Stretched Flames," Proceedings of the Twenty-Second Symposium (International) on Combustion, pp. 1-65, The Combustion Institute, 1988.

[30] Huntzinger, G.O., and Rigsby, G.E., "HEI - A New Ignition System Through New Technology," SAE paper 750346, 1975.

[31] Witze, P.O., and Vilchis, F.R., "Stroboscopic Laser Shadowgraph Study of the Effect of Swirl on Homogeneous Combustion in a Spark-Ignition Engine," SAE paper 810226, 1981.

[32] Metghalchi, M., and Keck, J.C., "Burning Velocities of Air with Methanol, Isooctane, and Indolene at High Pressure and Temperature," Combustion and Flame, Vol. 48, pp. 191-210, 1982.

[33] Liou, T.-M., Hall, M., Santavicca, D.A., and Bracco, F.V., "Laser Doppler Velocimetry Measurements in Valved and Ported Engines," SAE paper 840375, 1984.

[34] Fraser, R.A., Felton, P.G., Bracco, F.V., and Santavicca, D.A., "Preliminary Turbulence Length Scale Measurements in a Motored IC Engine," SAE paper 860021, 1986.

Appendix A

TIMING ELECTRONICS

A schematic diagram of the timing electronics used in the experiment is shown in Figure 48. The purpose of the circuit was to synchronize the sparking event with an analog to digital converter used to record the electrical characteristics of the spark. The circuit consists of a series of 555 timer chips, and 74121 monostable multivibrators. These chips are adjusted to produce three output signals of five volts with five milliseconds pulse widths, two of which are delayed outputs.

The circuit is initiated when a momentary normally open switch is activated. This process produces the first output pulse which immediately occurs following switch opening. The delayed outputs, set via the 4.0 K and 10 K potentiometers, can be varied to either coincide with the initial output or be independently delayed up to twelve milliseconds following the first signal.

The purpose of the first output signal was to initiate the sparking event. The second signal, delayed 4.9 milliseconds after the first, triggered the analog to digital converter. The last signal was a backup signal in case of failure of the first two signals.

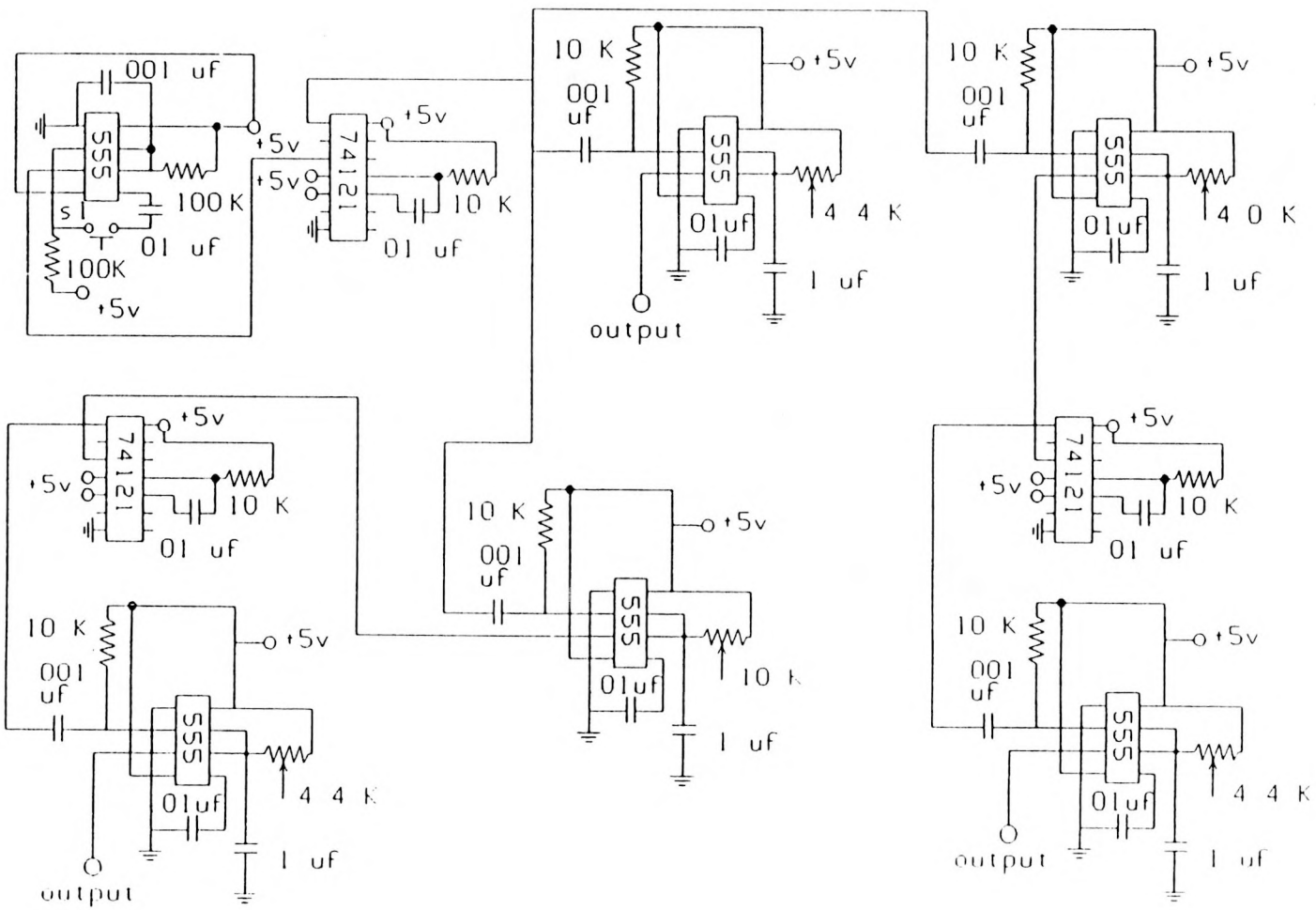

FIGURE 48: Timing electronics.

Appendix B

INDIVIDUAL KERNEL RADII CURVES

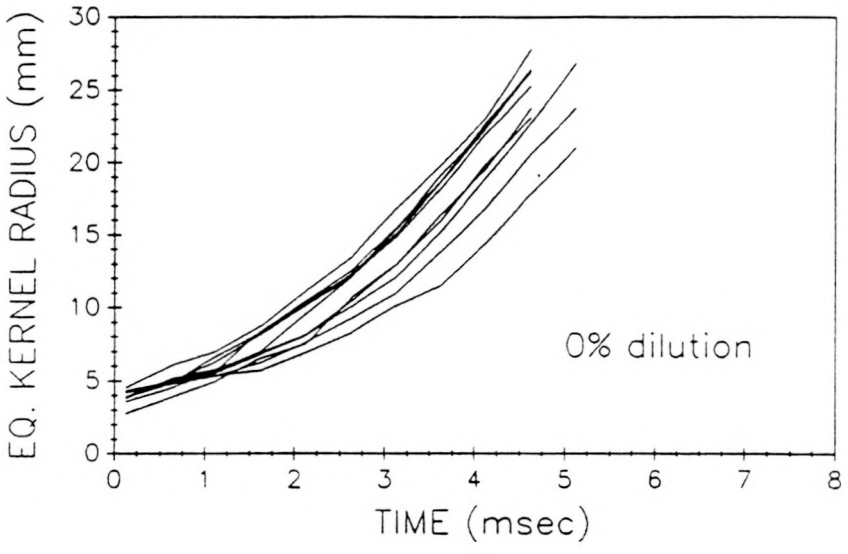

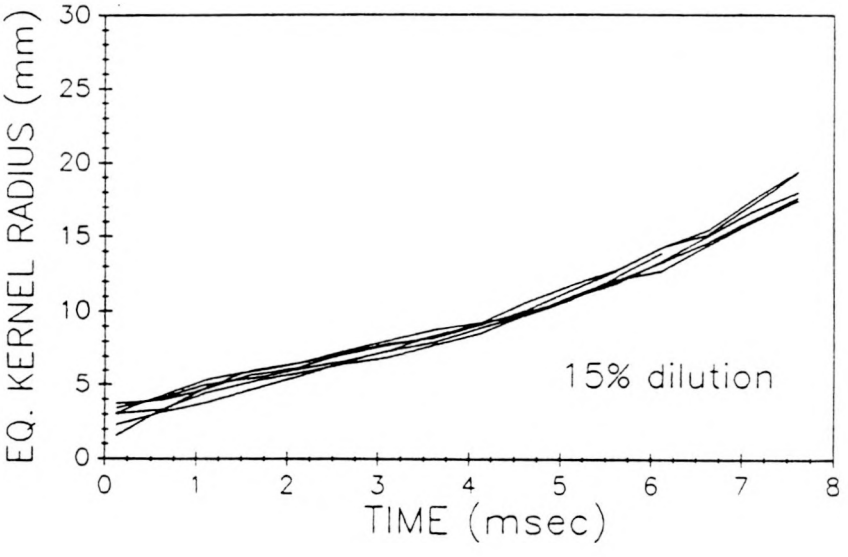

FIGURE 49: Individual kernel radii vs. time, 0% and 15% dilution, for the standard HEI effective energy 4.98 mJ, u'=.30 m/sec.

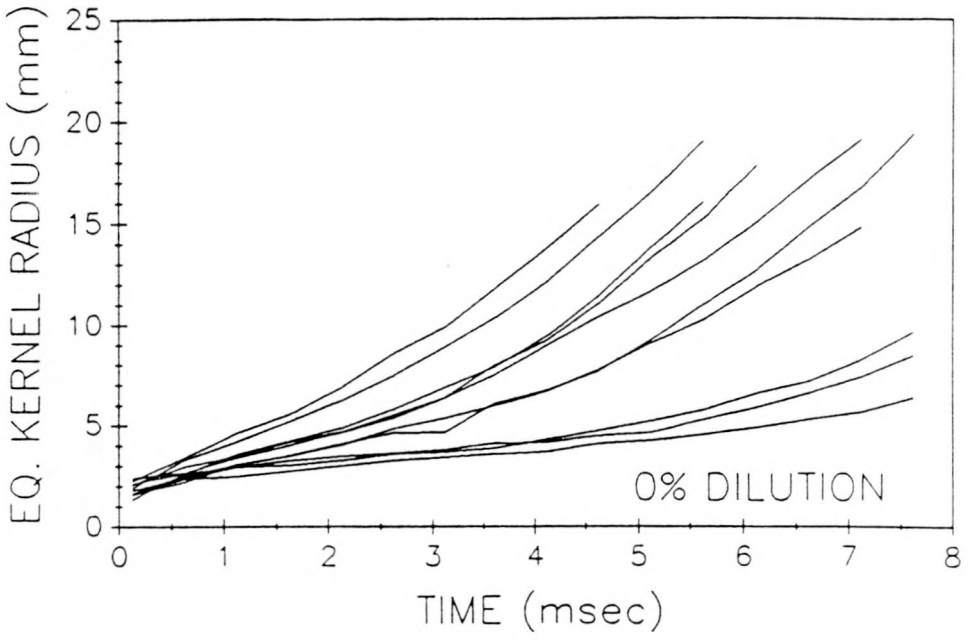

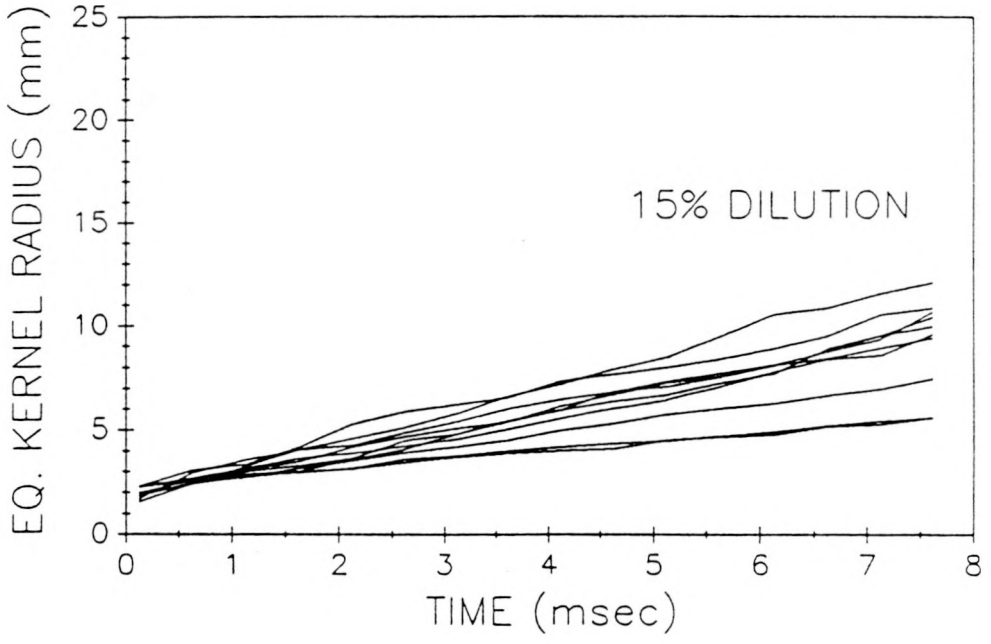

FIGURE 50: Individual kernel radii vs. time, 0% and 15% dilution, for the standard HEI effective energy 4.98 mJ, u'=.96 m/sec.

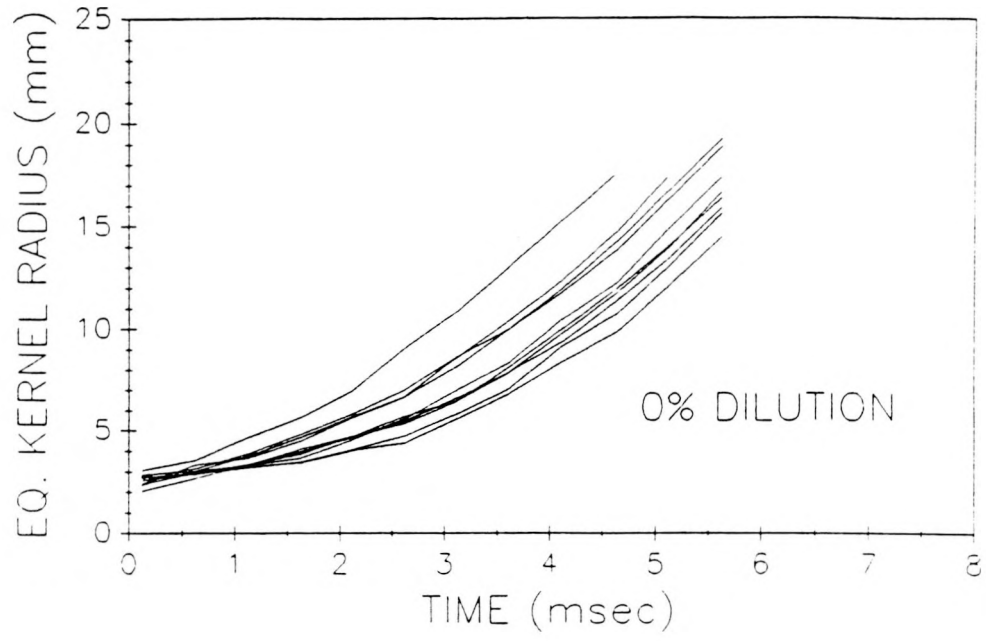

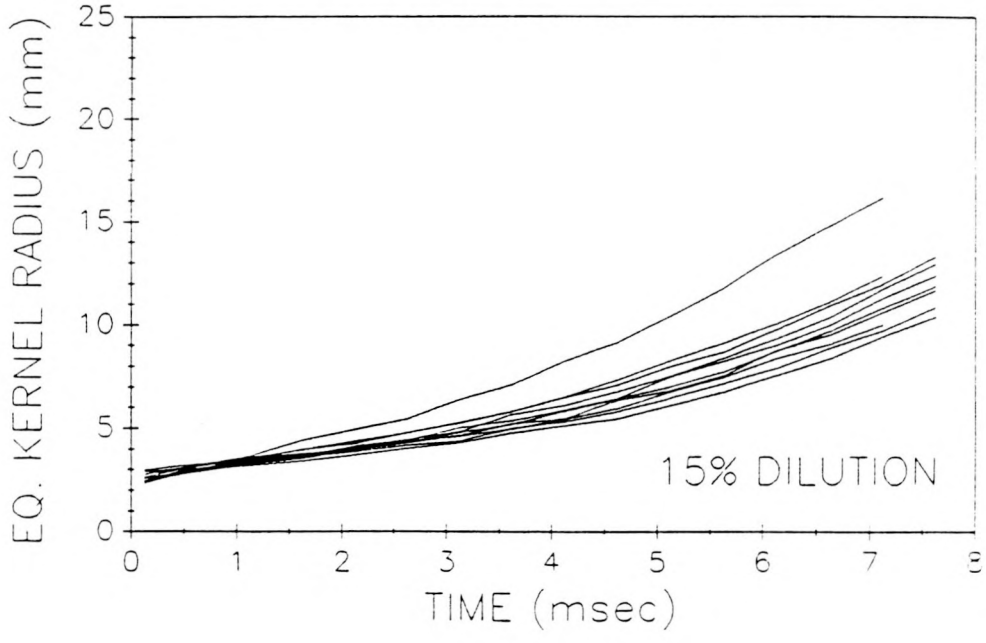

FIGURE 51: Individual kernel radii vs. time, 0% and 15% dilution, for the capacitive HEI effective energy 4.81 mJ, u'=.30 m/sec.

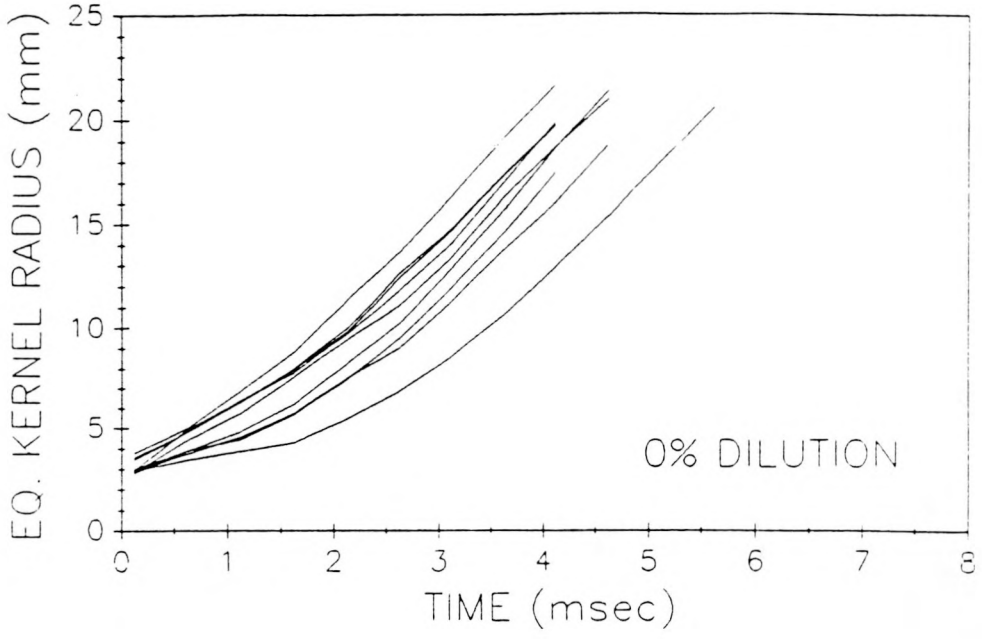

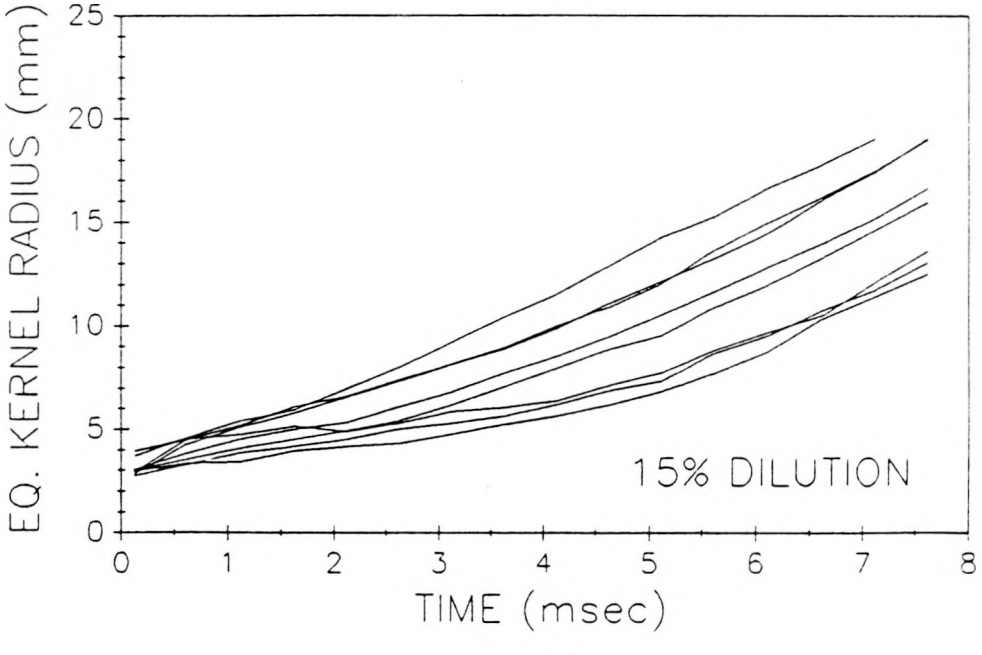

FIGURE 52: Individual kernel radii vs. time, 0% and 15% dilution, for the breakdown HEI effective energy 8.24 mJ, u'=.30 m/sec.

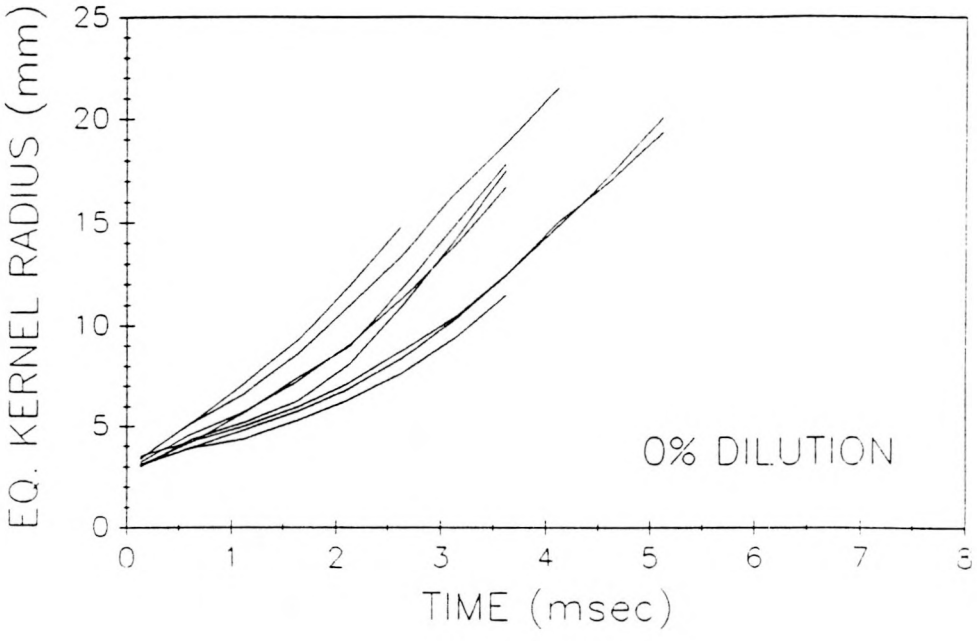

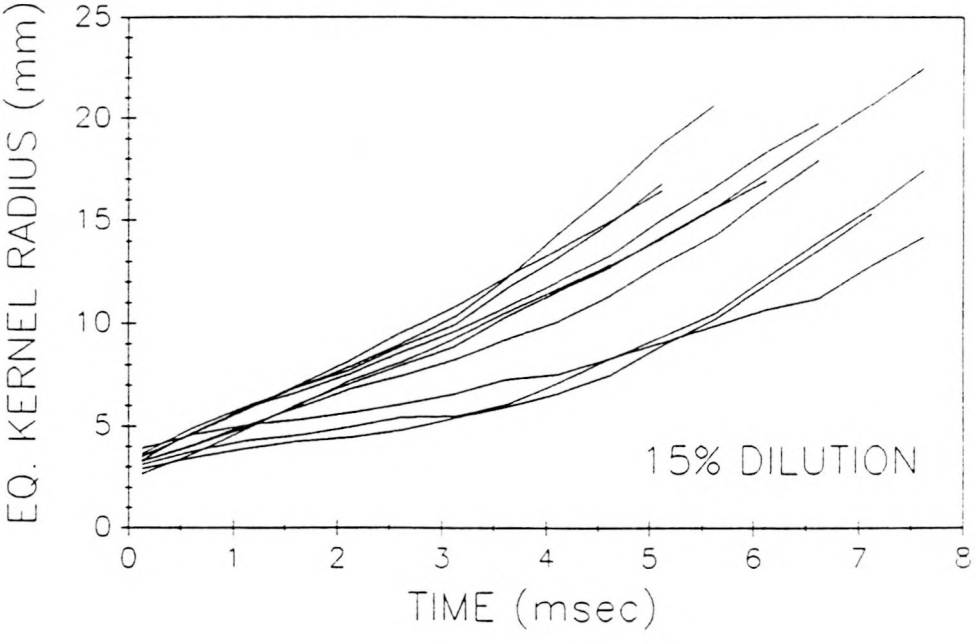

FIGURE 53: Individual kernel radii vs. time, 0% and 15% dilution, for the breakdown HEI effective energy 8.24 mJ, u'=.96 m/sec.